



The Canadian space agency planetary analogue materials suite



Edward A. Cloutis^a, Paul Mann^a, Matthew R.M. Izawa^a, Daniel M. Applin^a, Claire Samson^b, Roman Kruzelecky^c, Timothy D. Glotch^d, Stanley A. Mertzman^e, Karen R. Mertzman^e, Timothy W. Haltigin^f, Christopher Fry^b

^a Hyperspectral Optical Sensing for Extraterrestrial Reconnaissance Laboratory, Department of Geography, University of Winnipeg, 515 Portage Avenue, Winnipeg, Manitoba, Canada R3B 2E9

^b Department of Earth Sciences, Carleton University, Ottawa, ON, Canada K1S 5B6

^c MPB Communications, 147 Hymus Blvd, Pointe-Claire, QC, Canada H9R 1E9

^d Department of Geosciences, Stony Brook University, Stony Brook, NY 11794-2100, USA

^e Franklin & Marshall College, Department of Earth and Environment, Lancaster, PA 17604-3003, USA

^f Canadian Space Agency, John H. Chapman Space Centre, 6767 Route de l'Aéroport Saint-Hubert, Quebec, Canada J3Y 8Y9

ARTICLE INFO

Article history:

Received 8 September 2014

Received in revised form

14 August 2015

Accepted 2 September 2015

Available online 30 September 2015

Keywords:

Analogue materials

Mars

Surface

Moon

Surface

Impacts

Field-portable instruments

Spectroscopy

ABSTRACT

The Canadian Space Agency (CSA) recently commissioned the development of a suite of over fifty well-characterized planetary analogue materials. These materials are terrestrial rocks and minerals that are similar to those known or suspected to occur on the lunar or martian surfaces. These include: Mars analogue sedimentary, hydrothermal, igneous and low-temperature alteration rock suites; lunar analogue basaltic and anorthositic rock suites; and a generic impactite rock suite from a variety of terrestrial impact structures. Representative thin sections of the materials have been characterized by optical microscopy and electron probe microanalysis (EPMA). Reflectance spectra have been collected in the ultraviolet, visible, near-infrared and mid-infrared, covering 0.2–25 μm . Thermal infrared emission spectra were collected from 5 to 50 μm . Raman spectra with 532 nm excitation, and laser-induced fluorescence spectra with 405 nm excitation were also measured. Bulk chemical analysis was carried out using X-ray fluorescence, with Fe valence determined by wet chemistry. Chemical and mineralogical data were collected using a field-portable Terra XRD–XRF instrument similar to ChemMin on the MSL Curiosity rover. Laser-induced breakdown spectroscopy (LIBS) data similar to those measured by ChemCam on MSL were collected for powdered samples, cut slab surfaces, and as depth profiles into weathered surfaces where present. Three-dimensional laser camera images of rock textures were collected for selected samples.

The CSA intends to make available sample powders (< 45 μm and 45–1000 μm grain sizes), thin sections, and bulk rock samples, and all analytical data collected in the initial characterisation study to the broader planetary science community.

Aiming to complement existing planetary analogue rock and mineral libraries, the CSA suite represents a new resource for planetary scientists and engineers. We envision many potential applications for these materials in the definition, development and testing of new analytical instruments for use in planetary missions, as well as possible calibration and ground-truthing of remote sensing data sets. These materials may also be useful as reference materials for cross-calibration between different instruments and laboratories. Comparison of the analytical data for selected samples is useful for highlighting the relative strengths, weaknesses and synergies of different analytical techniques.

Crown Copyright © 2015 Published by Elsevier Ltd. All rights reserved.

1. Introduction

Given the relative rarity of many extraterrestrial materials, it can be difficult to acquire samples in sufficient quantities for many

applications, particularly those that involve consumption, alteration, or destruction of materials. Therefore, there is a need for well-characterized materials that can be used as analogues for extraterrestrial materials in the design, testing, and validation of instrument performance for planetary exploration missions, and for cross-checking the results of different instruments against standard materials similar to the real mission targets (e.g., Allen et al., 1981; Bost et al., 2013).

E-mail addresses: e.cloutis@uwinnipeg.ca (E.A. Cloutis), paul.mann347@gmail.com (P. Mann), matthew.izawa@gmail.com (M.R.M. Izawa).

Table 1

| | General description | Locality | Mineralogy (synthesis of XRD, XRF, optical and EPMA data) |
|-----------------------------|-------------------------------|---------------------------|----------------------------------------------------------------------------------------------------------------------------------------|
| <i>Mars sedimentary</i> | | | |
| CLA005 | Clay | Pembina Valley, MB | sed/alt Very poorly crystalline dominantly 2:1 layered clay with trace quartz |
| MAF700 | Silica | Mafeking, MB | sed/alt Amorphous silica with trace quartz and calcite |
| GYP160 | Gypsum | Gypsumville, MB | min Nearly pure gypsum |
| GYP161 | Gypsum | Gypsumville, MB | min Nearly pure gypsum |
| NON103 | Nontronite | Uley Mine, S. Australia | min Nearly pure nontronite |
| MON104 | Montmorillonite | Apache Co., AZ | min Nearly pure montmorillonite |
| SPT162 | Epsomite | Synthetic | min Synthetic epsomite, partial dehydration to starkeyite |
| NL-105 | Tufa | Tablelands, NL | sed/alt Fine-grained serpentine and calcite, Fe-oxyhydroxide stained |
| BSH012 | Tufa | Big Spring Hill, AB | sed/alt Fine-grained and granular, dominantly calcite with minor quartz |
| SPT158 | Na-sulphates | Chaplin, SK | min Dominated by thenardite |
| KA0104 | Kaolinite | Warren Co., GA | min Fine-grained kaolinite |
| <i>Mars hydrothermal</i> | | | |
| ASB003 | Serpentinite | Norbestos, QC | sed/alt Serpentine, magnetite, quartz, apophyllite |
| ASB230 | Serpentinite | Jeffrey Mine tailings, QC | sed/alt Serpentine, magnetite, quartz, gibbsite |
| ASB601 | Serpentinite | Normandie tailings, QC | sed/alt Serpentine, trace magnetite |
| ASB902 | Carbonated serpentinite | East Broughton, QC | sed/alt Talc, dolomite, minor serpentine |
| ICE003 | Silica sinter | Geysir, Iceland | sed/alt Amorphous silica, including hydrous silica |
| SIL304 | Tufa | Waiotupu, New Zealand | sed/alt Elemental sulphur with angular quartz fragments |
| NS-103 | Altered basalt | Blomidon Park, NS | sed/alt Plagioclase and pyroxene, zeolite-filled vugs |
| GYP316 | Pseudotachylite | Gypsumville, MB | imp Cryptocrystalline-glassy groundmass with quartz, chlorite, gypsum and amphibole |
| <i>Mars low-temperature</i> | | | |
| HAL001 | Halloysite | Tintic District, UT | min Mixture of halloysite-7 Å, halloysite-10 Å, trace kaolinite |
| VER104 | Vermiculite | Unknown | min Mixture of true vermiculite with its precursors biotite and chlorite; minor plagioclase |
| HAW049 | Palagonite | Mauna Kea, HI | sed/alt Mixture of gel-palagonite and fibro-palagonite, some relict pyroxene and plagioclase, heavily stained by Fe-oxyhydroxides |
| JSC-Mars1A | Palagonite | NASA/Hawaii | sed/alt Palagonitic material with relict plagioclase and pyroxene, heavily stained by Fe-oxyhydroxides |
| HEM104 | Haematite | Unknown | min Nearly monomineralic haematite, with trace quartz |
| CRB131 | Hydrothermal calcite | Axel Heiberg Island | min Monomineralic colourless calcite |
| CMB9 | Mine tailings | Central Manitoba mine | sed/alt Chlorite, quartz, gypsum, plagioclase, argentopentlandite |
| PRC001 | Fe-perchlorate | Synthetic | min Synthetic Fe(II) perchlorate hexahydrate (Alfa Aesar), possible alteration products (ferric compounds, different hydration states) |
| PRC003 | Mg-perchlorate | Synthetic | min Synthetic Mg-perchlorate anhydrous (Alfa Aesar), with some hydrated phases (2,4, and 6-hydrates) |
| NL-110 | Serpentinite from ophiolite | Tablelands, NL | sed/alt Serpentine, trace relict olivine |
| NL-116 | Weathered ophiolite sediments | Tablelands, NL | sed/alt Serpentine, trace relict olivine, quartz, albite |
| <i>Mars igneous</i> | | | |
| HAW006 | Basalt | Kohala, HI | vol Plagioclase, clinopyroxene, trace oxides (titanomagnetite) in glassy groundmass |
| HAY020 | Andesite | Hayden Butte, AZ | vol Plagioclase, K-feldspar, clinopyroxene and hornblende, minor chlorite, quartz and calcite |
| ICE170 | Pillow basalt | Iceland | vol Glassy groundmass with microlites of plagioclase, large olivine phenocrysts and subhedral chromite |
| OLV003 | Olivine mantle xenolith | San Carlos, AZ | int ig Monomineralic forsteritic olivine |
| PSA004 | Basalt | NASA JSC | vol Palagonitic material with relict plagioclase and pyroxene, heavily stained by Fe-oxyhydroxides |
| GRC007 | Dacite | Methana, Greece | vol Glassy groundmass, plagioclase and hornblende phenocrysts |
| MSH-ASH | Volcanic ash | Mt. St. Helens, WA | vol Glass-rich fragmental material, plagioclase and cristobalite detected by XRD |
| <i>Lunar basaltic</i> | | | |
| SA-20 | Basalt | Columbia River, OR | vol Glassy groundmass, plagioclase, clinopyroxene, magnetite |
| MAI203 | Ilmenite | Ivry Pit, QC | min Ilmenite, haematite exsolution lamellae, some albite and annite (Fe-rich biotite) |
| FJS-1 | Lunar mare simulant | Mt. Fuji, Japan | sed/alt Fragmental material with plagioclase, clinopyroxene |
| BAS600 | Ilmenite-bearing basalt | Minnesota | vol |
| PSA003 | Mars soil simulant | NASA JSC | sed/alt Glassy fragmental material with plagioclase, olivine, and clinopyroxene |
| HAW063 | Basalt | Hawaii | vol Glassy groundmass with plagioclase and clinopyroxene |

Table 1 (continued)

| | General description | Locality | Mineralogy (synthesis of XRD, XRF,optical and EPMA data) |
|---------------------------|-------------------------|----------------------------------------------------------------------------------------------------------|----------------------------------------------------------|
| <i>Lunar anorthositic</i> | | | |
| MAI001 | Anorthosite | St. Adele, QC | int ig |
| PSA001 | Lunar highlands simulat | NORCAT | sed/alt |
| PLG122 | Anorthosite | California, USA | int ig |
| CHX009 | Anorthosite | Charlevoix crater, QC | int ig |
| Shimizu-HS | Simulant | Shimizu Corp./JAXA | int ig |
| <i>Impactites</i> | | | |
| HMP-05-026 | Carbonate impact melt | carbonate (calcite and dolomite) clasts in fine-grained matrix of calcite and dolomite with minor quartz | imp |
| CM065 | Anorthosite impact melt | Mistastin crater, NL | imp |
| W05-41 | Shocked anorthosite | Mistastin crater, NL | imp |
| STM030 | Unshocked granite | St. Martin crater, MB | int ig |
| STM003 | Shocked granite | St. Martin crater, MB | imp |
| STM889 | Granite impact melt | St. Martin crater, MB | imp |

sed/alt=sedimentary or altered rocks; min=monomineralic samples; vol=volcanic rocks; int ig=intrusive igneous rocks; imp=impactites.

Recently, the Canadian Space Agency (CSA) commissioned the production of a suite of planetary analogue materials, including rocks and minerals representative of a range of lunar and martian settings and a suite of terrestrial impactites. Largely inspired by the International Space Analogue Rockstore (ISAR; see Bost et al., 2013), the CSA analogue materials suite aims to provide samples to the planetary science community to mature a variety of scientific and technological activities. Specifically, we envision that these samples will be useful for:

- (1) Investigating and refining science questions that may be asked of future missions;
- (2) Defining the necessary measurements to answer these questions, and in turn developing instrument requirements;
- (3) Assessing the performance of instrument breadboard or prototypes;
- (4) Maximising the scientific return of future missions by assessing results of various instrument combinations.

Given the relatively small quantities of the available material (few hundreds of grams), it is expected that their main use will be for instrument performance validation and testing. While acquisition policies related to the collection are not yet finalised, researchers interested in accessing this sample collection are encouraged to contact the Canadian Space Agency.

The ISAR group comprises a breadth of expertise in sample selection, curation, distribution, and investigation. For example, the utility of analogue sample suites for science investigation refinement was recently demonstrated by Bost et al. (2015), who interrogated two ISAR samples using elements of the ExoMars 2018 payload. Given the group's proven experience, it is anticipated that CSA will seek collaboration to investigate potential complementarities between the collections.

In this paper, we describe the mineralogical, chemical, textural and spectroscopic properties of the CSA planetary analogue materials suite. We highlight some of the potential uses of these materials for current and future planetary mission development and the validation of remote sensing data. Samples were selected based on similarity in spectral properties and inferred mineralogy and composition. The aim of this study was to create a set of analogue materials in large (> 100 g) quantities that would be comprehensively characterized and complement other collections

(e.g., ISAR) and sources of materials (e.g., NASA Astromaterials Facility). Many of material types inferred to be present on Mars (e.g., phyllosilicate-rich deposits, silica-rich materials, sulphates) are either not present, or present in sub-milligram quantities, in known martian meteorites. Therefore, terrestrial materials were used that match, as closely as possible, the mineralogical, geochemical, and spectral properties of the known or inferred extra-terrestrial 'target materials'.

The analogue materials suite is broadly divided into martian analogue, lunar analogue, and impactite subgroups. It should be noted that some of the igneous rock samples are applicable to both Mars and the Moon, but were assigned to one category or the other depending on which body was deemed to be most relevant. The subgroups are described in the following section, along with a brief summary of the geological background for each subgroup. The identities, provenance, and basic mineralogical character of each sample are summarised in Table 1. The sample nomenclature follows the nomenclature used by our lab (Planetary Spectrophotometer Facility) which will serve as an additional conduit for sample information; the PSF web site is <http://psf.uwinnipeg.ca>.

1.1. Mars

The martian surface contains a wide diversity of terrains, as revealed in the latest Geologic Map of Mars (<http://pubs.usgs.gov/sim/3292/>). The surface of Mars is composed largely of mafic igneous rocks (intrusive and volcanic) composed predominantly of olivine, pyroxene, and plagioclase feldspar (McSween and Treiman, 1998; Hamilton and Christensen, 2005; Milam et al., 2007; Rogers et al., 2007; Rogers and Christensen, 2007; Koeppen and Hamilton, 2008; McSween et al., 2009; Milam et al., 2010). A variety of secondary processes have physically and chemically altered the primary igneous materials of the martian crust resulting in a diversity of secondary mineral assemblages (Hurlowicz et al., 2006; Leshin and Vicenzi, 2006; Ming et al., 2006; Arvidson et al., 2008; Knoll et al., 2008; McLennan et al., 2013; Williams et al., 2013). The martian surface also contains abundant windblown dust that is derived from the physical and chemical weathering of these volcanic rocks (e.g., Hamilton et al., 2005).

While mafic rocks of basaltic affinity are the most areally abundant martian rocks, and are the only types of rocks represented in martian meteorites, the less abundant rocks and

minerals are of greater scientific interest. In particular, sedimentary rocks are of very high interest because they: (1) occur in some of the oldest terrains on Mars, and hence have a higher probability of preserving microbial life, and also indicate that conditions on Mars were possibly more Earth-like than at present (e.g., Williams et al., 2013); and (2) contain water-bearing minerals (Grotzinger et al., 2013; McLennan et al., 2013; Ming et al., 2013; Vaniman et al., 2013). In addition, some martian surface deposits contain minerals precipitated or metasomatised by hydrothermal solutions (Morris et al., 2008; Squyres et al., 2008), with important implications for habitability, as hydrothermal systems generated by endogenic or exogenic heat sources are very suitable environments for microbial life (e.g., Brock, 1967; Cockell and Lee, 2002). It is worth noting that Gale crater, currently explored by the Mars Science Laboratory (MSL) Curiosity rover, consists of basaltic volcanic rocks, concentrations of mafic minerals (olivine, pyroxene), along with clays and sulphates (Blake et al., 2013; Grotzinger et al., 2013; Johnson et al., 2013; McLennan et al., 2013; Vaniman et al., 2013).

Martian geology is too diverse to include all known or suspected rock and mineral types in this study. We have focused on sedimentary rocks and alteration products (of low-temperature weathering and hydrothermal activity), because of the high scientific interest stemming from their interaction with water and their potential for preserving evidence of past life and acting as paleoenvironmental indicators (Fernandez-Remolar et al., 2009; McLennan et al., 2013; Williams et al., 2013). Some common igneous rocks and minerals are included because they represent the protolith compositions and basement lithologies for sedimentary and altered rocks.

1.1.1. Mars sedimentary rock suite

Orbital imagery and spectroscopy indicate that Mars has a wide variety of physical and chemical sediments, and that their distribution reflects a mixture of aeolian, fluvial-lacustrine, mass wasting, and other processes. The relationships between stratigraphic textures and sedimentary minerals have been established for many areas by linking imagery to mineralogy via orbital spectroscopy. This is bolstered by images from the surface showing both fine-grained sediments (e.g., subsurface soils of different colours exposed by the Spirit rover), as well as more consolidated sedimentary rocks (conglomerates) examined by MSL. Within the sedimentary rocks thus far identified on Mars, the most scientifically interesting minerals include: (1) Clays such as serpentine, nontronite, montmorillonite, and kaolinite (e.g., Clark et al., 2007; Mustard et al., 2008; Wray et al., 2008; McKeown et al., 2009; Ehlmann et al., 2011). All contain structural water and/or hydroxyl and can be used as indicators of paleoenvironmental conditions. (2) Sulphates such as hexahydrite, kieserite, and gypsum (e.g., Gendrin et al., 2005; McLennan et al., 2005; Bishop et al., 2008; Kounaves et al., 2010). These are also water-bearing and form, or are stable, under specific physicochemical conditions. (3) carbonates such as calcite, siderite, and magnesite (e.g., Bandfield et al., 2003; Ehlmann et al., 2008; Boynton et al., 2009; Palomba et al., 2009; Michalski and Niles, 2010; Morris et al., 2010). While not all water-bearing, these minerals are generally associated with formation in hydrous environments, and are indicative of environmental conditions. (4) Iron oxyhydroxides such as haematite, magnetite and goethite (e.g., Glotch et al., 2004; Morris et al., 2006; Squyres et al., 2006; Morris et al., 2008). These minerals can be indicative of previous environmental conditions, and appear to be widespread on Mars, particularly in windblown dust and weathering rinds exposed at the surface (the red colour of Mars derives largely from fine-grained haematite). The importance of these minerals as evidence for water on Mars and as tracers of past environmental conditions can be seen from the criteria used for

landing site selection of recent Mars missions (Pathfinder: an area of presumed large-scale water flows; Phoenix: an area of presumed near-surface ice; Spirit: an area (Gusev crater) presumed to have once hosted a lake; Opportunity: an area presumed to have once hosted standing water; Curiosity: an area of sedimentary rocks presumed to have recorded gradual change in Mars environmental conditions).

1.1.2. Mars hydrothermally altered rock suite

Several types of hydrothermal activity are likely to be important in the alteration of the martian crust. Among these are magmatic hydrothermal systems driven by intrusive or extrusive igneous activity; impact-related hydrothermal systems where fluid circulation is driven by heating due to hypervelocity impact, low-temperature systems driven by exothermic chemical reactions such as serpentinization (Oze and Sharma, 2005; Viviano et al., 2013) and possibly others (e.g., Schwenzer and Kring, 2009; Schwenzer et al., 2012).

1.1.3. Mars low-temperature altered rock suite

Hydrothermal alteration occurs over a wide range of temperatures and there is no consensus on the temperature boundary between aqueous and hydrothermal alteration. On Mars, low-temperature alteration may or may not involve fluids. The previously described Mars hydrothermal alteration suite spans materials formed over the range from ~150 to 500 °C. In addition to fluid-assisted alteration, Mars materials may undergo fluid-free or fluid-limited alteration, particularly at low temperatures, akin to alteration that occurs in polar environments (Knoll et al., 2008; Morris et al., 2008; Salvatore et al., 2014).

There is also growing evidence for low-temperature sulphuric acid-assisted alteration of rocks and mineral grains (e.g., Squyres et al., 2004; McLennan et al., 2005; Squyres and Knoll, 2005; Tosca et al., 2005; Niles and Michalski, 2009), particularly in the north polar regions of the planet (Horgan et al., 2009). This alteration results in the formation of silica-rich rinds on rock and mineral grain surfaces. In addition, there are many silica-rich deposits on Mars that likely formed under conditions intermediate between hydrothermal and low-temperature (Squyres et al., 2008; Rice et al., 2009).

1.1.4. Mars igneous rock suite

Spectral observations from martian orbit (e.g. Mars Express Orbiter) and from surface rover analysis (Sojourner, Spirit and Opportunity) have led to the view that the martian surface is dominantly basaltic, consisting mainly of tholeiites and highly weathered basalts formed by partial melting of the mantle (e.g., Squyres et al., 2006; Arvidson et al., 2008; Rogers and Aharonson, 2008; McSween et al., 2009). Martian meteorites provide ground truth that basaltic materials dominate the martian surface. The major martian meteorite groups include chassignites (olivine-rich cumulate rocks), nakhlites (clinopyroxene-rich cumulate rocks) and shergottites (basalts) (e.g., McSween and Treiman, 1998). The shergottites can be further subdivided into subtypes, but these are largely small variations on a theme (i.e., they are basalts or closely-related rocks) (McSween and Treiman, 1998; Nyquist et al., 2001). In a few restricted locations on Mars, analyses of orbital spectra indicate the presence of more evolved igneous rocks, possibly ranging up to granitic in composition (Bandfield et al., 2004; Christensen et al., 2005), though the effects of alteration can interfere with this interpretation (Hamilton et al., 2003). The origin mechanisms of more evolved igneous rocks on Mars remains highly uncertain, especially given the current lack of any physical samples (i.e., meteorites) having substantially evolved compositions.

1.2. Moon

In contrast to the surface of Mars, the surface of the Moon is dominated by two main geological regions: (1) highlands, which consist predominantly of anorthitic plagioclase-rich assemblages; and (2) mare, which are composed largely of basalts. Within each of these regions there are some compositional variations. For instance, the highlands include rock types containing variable proportions of minerals such as plagioclase feldspar, olivine (notably as a component of the intrusive magnesian suite, and possibly as exhumed mantle material), and orthopyroxene, and these minerals also exhibit variations in composition, such as the so-called alkali suite containing more sodic plagioclase, (e.g., Keil et al., 1970; Wakita and Schmitt, 1971; Ringwood and Green, 1972; Yamamoto et al., 2010). Mare basalts include subtypes with variable proportions of plagioclase feldspar, olivine, clinopyroxene, and ilmenite, also with compositional variations within each of these minerals. In addition to these major rock types, lunar regolith also contains several glass phases of both impact and volcanic origin (e.g., Wells et al., 1972; Wells and Hapke, 1977; Korotev, 1991; Korotev et al., 2010), and agglutinates (glass-welded fragments) produced by micrometeoroid bombardment (Steele and Smith, 1973; Papike et al., 1998). Some areas of the Moon are partly covered by pyroclastic glass: fine-grained glass beads produced by volcanic eruptions (Gaddis et al., 1985). Many lunar samples contain a late differentiation product enriched in incompatible elements generally referred to as KREEP (potassium, rare earth element and phosphorous) (Keil et al., 1975; Haskin et al., 2000). Recent remote sensing observations have also indicated the presence of a spinel–orthopyroxene–olivine assemblage, the abundance of which, while limited, has important petrogenetic implications (Pieters et al., 2011); as well as spinel-bearing lithologies that are relatively free of mafic components (Dhingra et al., 2011; Pieters et al., 2014). The large-scale lithology of the Moon is the result of its formation process. Anorthositic bodies corresponding to the modern highlands formed via floatation in a magma ocean. Later impact and volcanic processes led to the emplacement of mare basalts in (predominantly) nearside impact basins, with variable incorporation of KREEP, the last differentiate of the lunar magma ocean (Walker and Hays, 1977; Haskin et al., 2000; Jolliff et al., 2000; Korotev and Gillis, 2001).

The lunar surface or near-surface, particularly in the Polar Regions, may also contain deposits or concentrations of water ice, concentrated in permanently shadowed regions (Spudis et al., 2010). The detection of widespread hydration of the lunar surface by multiple spacecraft instruments has strengthened the case for an important role of volatiles including hydroxyl and molecular water in the lunar surface (Pieters et al., 2009; Sunshine et al., 2009; McCord et al., 2011). Analyses of the volatile contents of the lunar interior have also revealed the presence of hydration (e.g., Saal et al., 2008; McCubbin et al., 2010). Near-surface deposits of hydrous material, especially water ice, are of interest as *in situ* sources of water, oxygen, and hydrogen to support an extended human presence on the Moon.

1.2.1. Lunar anorthositic suite

The light regions of the Moon consist of rocks that are dominated by anorthitic plagioclase feldspar. Recent remote sensing observations and detailed investigations of lunar meteorites indicate that while the majority of the lunar highlands are composed of high-Ca anorthite (Ohtake et al., 2009), there are substantial variations in composition (Korotev et al., 2003; Cahill et al., 2004; Glotch et al., 2010; Greenhagen et al., 2010; Seddio et al., 2013). Besides Ca-rich plagioclase, the anorthositic highland rocks contain variable amounts of olivine, clinopyroxene, and orthopyroxene (e.g., Wakita and Schmitt, 1971; Dowty et al., 1974; Bersch

et al., 1991; Korotev, 1991; Norman et al., 1991; Korotev and Morris, 1993; Korotev et al., 2009).

1.2.2. Lunar basaltic suite

Basalts make up the majority of the Moon's "dark" regions, occurring largely as fill of larger impact basins, predominantly on the nearside (e.g., Lucey, 2004). Lunar basalts are chemically very reduced and volatile-depleted compared to terrestrial or martian basalts, but are broadly similar in bulk composition and mineralogy (e.g., Papike 1998; Papike et al., 2003; Korotev, 2005). Lunar basalts are dominated by clinopyroxene and plagioclase feldspar, with lesser orthopyroxene and oxide minerals including ilmenite, magnetite, and Cr-spinel (e.g., Papike et al., 1998; Papike et al., 2003; Korotev, 2005). While lunar basalts also contain a number of phases (e.g., armalcolite, tranquillityite) that are absent in most terrestrial and martian basalts, these components are typically very rare and, while important for trace-element and isotopic studies, should not affect first-order lithological and physical properties.

1.3. Impactites

Hypervelocity impact is a process common to all solid planetary surfaces. Both the lunar and martian surfaces have been affected by impacts over a range of scales. Impacts can affect planetary surfaces in a number of ways. Immediate effects include heating, melting, vapourization, and brecciation of target rocks, redistribution of rocks as ejecta and uncovering of subsurface rocks. Heat produced by impact can also lead to the development of hydrothermal systems in water-bearing targets. Impact-generated hydrothermal systems are of particular relevance for Mars, as a source of thermal and geochemical energy sources for microbial life (e.g., Abramov and Kring, 2005; Osinski et al., 2005; Izawa et al., 2011), as well as fracturing and changes in porosity that can affect the habitability of target rocks (Cockell et al., 2002; Cockell et al., 2003).

2. Methods

In order to provide a comprehensive data set, the rock and mineral samples comprising the CSA sample suite were characterized using a wide range of analytical techniques, emphasising techniques appropriate to different types of samples. Table 1 provides a list and description of the samples comprising the sample suite. Details of the applied analytical techniques are described below.

For the natural rock samples, 'parent' samples of ~30 g mass were pulverised and homogenised, then subdivided into aliquots in order to provide representative data. One aliquot (~20 g) was designated for reflectance, Raman, and fluorescence spectra and diffraction. Another (~5 g) was analysed by X-ray fluorescence, and a third (~5 g) was used in emission spectroscopic measurements. Synthetic materials (e.g., perchlorate salts), reference materials (e.g., clay mineral reference samples) and regolith simulants (e.g., NASA JSC-Mars-1) generally required no further homogenisation. For the two microanalytical methods, electron probe microanalysis and laser-induced breakdown spectroscopy, multiple points on thin sections and hand samples respectively were analysed, as detailed below.

2.1. Powder X-ray diffraction (XRD) – Bruker D8 Advance

Samples were crushed to fine powder with alumina mortars and pestles, and dry sieved to < 45 µm. X-ray diffraction data were collected in continuous scan mode from 5° to 70° 2θ with a

Bruker D8 Advance DaVinci automated powder diffractometer. The diffractometer was operated in Bragg–Brentano geometry and equipped with a 2.5° incident Soller slit, 1.0 mm divergence slit, a 2.0 mm scatter slit, a 0.6 mm receiving slit, and a curved secondary graphite monochromator. Diffracted X-rays were detected using a scintillation counter collecting at an increment of 0.02° with an integration time of 1 second per step. The line-focus Co X-ray tube (Co $K\alpha_{1,2}$ radiation, $\lambda=1.7902$ Å) was operated at 40 kV and 40 mA, using a take-off angle of 6°. Diffractograms were interpreted using the International Centre for Diffraction Data Powder Diffraction File (ICDD-PDF-2) database.

2.2. X-ray diffraction and fluorescence-Terra portable XRD/XRF

The Terra XRD analysis used subsamples of the same < 45 μm powders as in Section 2.1 (lab powder XRD) above. Both X-ray diffractograms and X-ray fluorescence spectra were acquired using an InXitu Terra 299 portable X-ray device with a 1024 \times 256 pixels – 2D Peltier-cooled CCD detector. The Terra instrument provides XRD data from 5 to 55° 2θ (Bragg angle) with 0.05° angular resolution, and XRF spectra covering 3 to 25 keV. X-rays are produced with a sealed Cu source (Cu $K\alpha_{1,2}$ radiation, $\lambda=1.5418$ Å) operating at 30 kV accelerating voltage and 10 W power. A total of 200 exposures were collected and averaged to increase signal-to-noise ratio. The Terra XRF–XRD instrument at the University of Winnipeg is a commercial version of the CheMin instrument on the MSL Curiosity rover (with a Cu rather than Co source).

2.3. Laboratory X-ray fluorescence (XRF)

Crushed rock powders (0.4000 g) were mixed with lithium tetraborate (3.6000 g), placed in a Pt: 5% Au crucible and heated over a Meker burner until molten. The molten material was then transferred to a platinum casting dish and quenched. This procedure produces a glass disk that is used for XRF analysis of major and selected minor elements. Elemental abundances were converted to equivalent oxides using the normal oxidation state of the various elements. Trace elements (Sr, Zr, V, Cr, Ni, and Co) are reported as parts per million (ppm). Working curves for each element are determined by analysing geochemical rock standards (Abbey, 1983). Between 30 and 50 data points are gathered for each working curve; various elemental interferences are also taken into account. Results are calculated and presented as percent oxide. Details of the experimental procedure can be found in Mertzman (2000).

2.4. Ferrous iron titration and loss on ignition (LOI)

The amount of ferrous iron is determined by titration using a modified Reichen and Fahey (1962) method. Ferric iron (Fe^{3+}) is determined as the difference between total iron (from lab XRF Section 2.3) and ferrous iron. Loss on ignition (which is a measure of volatile content) is determined by heating an exact aliquot of the sample at 950 °C in air for one hour and measuring the resultant weight loss.

2.5. Ultraviolet spectral reflectance (200–400 nm)

Ultraviolet reflectance (200–400 nm) spectra were measured with an Ocean Optics Maya2000 PRO miniaturised spectrometer equipped with an HC-1 grating and 30 μm slit width, giving an effective spectral resolution between 0.48 nm at 200 nm and 0.46 nm at 400 nm. The detector is a 2D back-thinned linear CCD-array. Illumination was provided by an Analytical Instrument Systems Inc. Mini-DTA light source with a 30 W deuterium lamp through a bifurcated fibre optic bundle consisting of six

illumination fibres surrounding a central pick-up fibre feeding into the detector array. The fibre optic bundle was used at normal incidence ($e=i=0^\circ$). All measurements were acquired with an integration time of 600 ms and 200 individual spectra were averaged together. The spectra were corrected to absolute reflectance by referencing each spectrum measured against a calibrated Spectralon[®] 100% diffuse reflectance standard to a deep ultraviolet (DUV) mirror. The DUV mirror correction removes irregularities in the Spectralon[®] standard using a calibrated mirror. These experimental procedures are based on those described by Cloutis et al. (2008).

2.6. Visible-near infrared reflectance spectra (400–1100 nm)

Visible and near infrared (400–1100 nm) reflectance spectra were measured with an Ocean Optics Maya2000 PRO miniaturized spectrometer equipped with an HC-1 grating and 30 μm slit width, providing an effective spectral resolution of ~ 0.46 nm between 400 and 1100 nm. The detector is a 2D back-thinned linear CCD-array. Illumination was provided by a 150 W quartz–tungsten–halogen collimated light source with a viewing geometry of $i=30^\circ$, $e=0^\circ$. Measurements for each sample were made by first acquiring a dark current spectrum (with the input to the spectrometer blocked), a reference spectrum, and a sample spectrum. All measurements were acquired relative to a Spectralon[®] 100% diffuse reflectance standard. An integration time of 13 ms was used, and each measurement consists of 500 individual spectra.

2.7. Ultraviolet-visible-near infrared reflectance spectra (350–2500 nm)

Long-wave ultraviolet, visible and near IR (350–2500 nm) reflectance spectra were measured with an Analytical Spectral Devices FieldSpec Pro HR spectrometer with a spectral resolution of between 2 and 7 nm (internally resampled by the instrument to 1 nm). Spectra were measured with incidence angle 30° and emergence angle 0°. Incident light was provided by an in-house 150 W quartz–tungsten–halogen collimated light source. Sample spectra were measured relative to a Spectralon[®] (Labsphere, North Sutton, NH) 100% diffuse reflectance standard and corrected for minor (less than $\sim 2\%$) irregularities in absolute reflectance. In each case, 200 spectra of the dark current, standard, and sample were acquired and averaged, to enhance the signal-to-noise ratio for subsequent interpretation. Some spectra showed occasional small reflectance offsets at 1000 and 1830 nm due to the fact that the fibre optics that feed the three detectors in the FieldSpec Pro spectrometer do not view the exact same locations on the surface of the sample. These offsets are corrected by scaling the short (350–1000 nm) and long wavelength (1830–2500 nm) detectors to the end points of the central detector, which is temperature controlled. Sample heterogeneity effects are minimised by the generally small particle size of the samples relative to the spectrometer field of view. For whole rock samples, and to a lesser extent the coarse powders (45–1000 μm particle size), some spectral variability may be ascribable to sample heterogeneity.

2.8. Infrared reflectance spectra (2.0–5.2 μm)

Reflectance spectra from 2.0–5.2 μm were collected with a Designs & Prototypes Model 102F spectrophotometer. Samples were illuminated with an in-house 150 W quartz–tungsten–halogen light source directed through an open-air aluminum pipe at 30° from normal. The spectrometer is equipped with a Designs & Prototypes customised optical assembly that allows a spot size of ~ 7 mm to be viewed by the instrument. The spectrometer uses a Michelson interferometer which contains the infrared optics,

beam splitter, and the scanning mirror assembly. The internal mirrors are servo driven at a constant speed to produce the interferograms. Spectral resolution for all measurements was 6 cm^{-1} . The InSb detector is thermo-electrically cooled detector (77 K). The servo, electronics, and wavelength calibration are referenced to a temperature controlled laser diode. Reflectance spectra were acquired relative to a Labsphere Infragold[®] diffuse gold-coated standard. Reference spectra were acquired with the same viewing geometry and illumination used for the samples and with the same number (100) of co-adds.

2.9. Mid-infrared emissivity spectra (200–2000 cm^{-1} ; 5–50 μm)

Emissivity spectra were acquired in an atmosphere purged of CO_2 and H_2O using the Stony Brook University Vibrational Spectroscopy Laboratory's Nicolet 6700 Fourier Transform infrared (FTIR) spectrometer, modified to collect emissivity spectra by switching off the Global thermal infrared light source and heating the sample to $80\text{ }^\circ\text{C}$ to increase the thermal emission of the sample (and thus increase the signal-to-noise ratio of the measurements). Each measurement is an average of 256 scans acquired over a period of about 8 minutes. Measured spectra were calibrated to emissivity using blackbody calibration targets (electric heaters) heated to $70\text{ }^\circ\text{C}$ and $100\text{ }^\circ\text{C}$, using the procedure of Ruff et al. (1997). The sample chamber was purged with dry, scrubbed N_2 in order to reduce or eliminate water vapour and CO_2 .

2.10. Raman spectroscopy

Raman spectra were collected in the Raman shift range of $175\text{--}4000\text{ cm}^{-1}$, at a typical spectral resolution of $\sim 4\text{ cm}^{-1}$ (at 614 nm), with a B&W Tek i-Raman-532-S instrument. Excitation was provided by a 532 nm $\sim 50\text{ mW}$ solid-state diode laser. Raman-scattered light was detected by a GlacierTM T, a high spectral resolution (0.08 nm) thermoelectrically cooled ($14\text{ }^\circ\text{C}$) CCD detector. The automatic integration time function (which increases integration time incrementally, until the response is close to saturation) was used, yielding an optimal signal-to-noise ratio. Raman-shift calibration was monitored through regular measurements of a polystyrene standard. Baseline correction was carried out using the automated baseline correction removal function in the BWSpec software, which operates as described by Baek et al. (2015). Background subtracted data have been included in the supplemental online material associated with this article.

2.11. Laser-induced fluorescence spectra (400–1100 nm)

Fluorescence spectra were measured with an Ocean Optics Maya2000 PRO miniaturized spectrometer operated in intensity mode. Illumination was provided by a 75 mW , 405 nm diode laser beam projected on to the sample. Fluorescent emission was directed to the detector through a fibre-optic cable using a viewing geometry of $i=0^\circ$ and $e=0^\circ$ (normal incidence). Spectra were collected in raw counts intensity mode and were not measured relative to a calibrated standard. The spectral data are therefore primarily useful for qualitative comparison of the fluorescence signatures of the various samples rather than for quantitative analysis.

2.12. Laser-induced breakdown spectroscopy (LIBS)

LIBS collection involved a pulsed laser with 1574 nm wavelength passed through a collimator followed by a dichroic filter where light at 1574 nm is transmitted and light between 200 nm and 850 nm is reflected. The laser beam is then focused on the sample. Because the pulse width of the laser is short and the focal

point is small, the intensity of the light is sufficient to thermally ablate the sample and generate plasma. The excited atoms and molecules within the plasma de-excite by electron-ion recombination and photon emission, and the emission spectra are characteristic of the sample composition. Emitted light was directed by a focusing lens through the dichroic filter, and focused on a bundle of fibre optics. Optical fibres then direct the light to four spectrometers covering wavelengths ranging between 200 and 850 nm . The four spectrometers are synchronized and the acquisition is taken with a small delay from the pulse to reduce background due to the plasma continuum emission.

Each sample was placed in the instrument focal plane, and 10 spectra were measured for each sample. Two different sets of samples were analysed, a set of $< 45\text{ }\mu\text{m}$ grain size powders, and a set of unprepared rock slabs. For the powders, the samples were moved slightly between each measurement, because holes were created on the samples by each laser pulse. For the slabs, two different methodologies were used depending on whether the sample had an exterior that was visually different from the unweathered interior. For the interior, the same approach as for powders was used. For the weathered exteriors, the sample was not moved between the shots (i.e., the 'weathered exterior' measurements are depth profiles). For each spectrum, the acquisition corresponds to a single laser pulse with an integration time of 3 ms .

2.13. Electron probe microanalysis (EPMA)

Electron probe microanalysis of major phases was carried out on polished thin sections of samples MAI210, STM030, NL110, ICE170, SA20, GYP316, MAI001, Shimizu HS, CM065, STM003, STM_889, CHX009, W05-41, HAW063 and HMP05-026. The analyses were carried out at the University of Alberta using a JEOL 8900 Electron Probe Microanalyzer. The sections were coated with a thin ($\sim 250\text{ \AA}$) layer of vacuum-deposited amorphous carbon for electrical conductivity. Analysis was carried out in wavelength-dispersive mode. Natural and synthetic standards were used for spectrometer calibration as follows: Si, Mg, and Ca on diopside, Ti on rutile, Al and K on sanidine, Cr on synthetic $\alpha\text{-Cr}_2\text{O}_3$, Fe on fayalite, Mn on rhodonite, Na on albite, and Ni on synthetic $\alpha\text{-Ni}^\circ$ (metal). Analyses of kaersutite, labradorite, and augite secondary standards were measured at the beginning, end, and intermittently during the analytical run to monitor instrument drift. An accelerating voltage of 15 kV and 20 nA beam current were used. Beam diameters of 2 nm were used for all phases except plagioclase and potassium feldspar, where a 5 nm defocused beam was employed to reduce alkali loss. Counting times were 30 s on peak and 15 s on background. Elemental abundances were corrected for sample matrix effects using standard EPMA procedures.

2.14. Optical microscopy

Optical petrographic analysis of polished thin sections was carried in transmitted, plane- and cross-polarised light using a Nikon Eclipse LV100 POL petrographic microscope equipped with a Nikon DS-Ri1 12 Mpixel camera. Additional observations were made for opaque phases using reflected light microscopy.

2.15. 3D imaging

A Konica-Minolta Vivid 9i non-contact 3D laser camera was used to image the whole-rock samples. This laboratory camera projects a visible (690 nm) laser on a sample and records the X, Y, and Z Cartesian coordinates of each illuminated point on the sample surface. It does not capture reflection intensity (albedo). An individual image is an unstructured "cloud" of points in 3D space

Table 2

| <i>Mars sedimentary</i> | | | | | | | | | | | |
|----------------------------------|--------|--------|--------|-------------|--------|--------|---------|--------|--------|--------|--------|
| | CLA004 | MAF700 | GYP160 | GYP161 | NON103 | MON104 | SPT162 | NL-105 | BSH012 | SPT158 | KAO104 |
| SiO ₂ | 82.21 | 97.92 | 2.07 | 0.00 | 56.08 | 67.03 | 0.00 | 26.33 | 12.93 | 1.94 | 51.61 |
| TiO ₂ | 0.38 | 0.02 | 0.01 | 0.00 | 0.56 | 0.25 | 0.00 | 0.01 | 0.05 | 0.03 | 2.49 |
| Al ₂ O ₃ | 9.19 | 0.35 | 0.25 | 0.00 | 4.89 | 19.75 | 0.01 | 1.06 | 1.83 | 0.45 | 44.67 |
| Fe ₂ O ₃ T | 3.58 | 0.41 | 0.33 | 0.06 | 34.87 | 1.73 | 0.04 | 5.25 | 0.56 | 0.14 | 11.15 |
| MnO | 0.25 | 0.00 | 0.01 | 0.00 | 0.01 | 0.10 | 0.01 | 0.06 | 0.02 | 0.01 | 0.01 |
| MgO | 1.48 | 0.01 | 1.14 | 0.04 | 0.98 | 6.97 | 29.68 | 23.21 | 1.31 | 0.10 | 0.11 |
| CaO | 0.80 | 0.39 | 41.66 | 42.71 | 1.79 | 3.37 | 0.06 | 43.36 | 81.97 | 0.30 | 0.02 |
| Na ₂ O | 0.28 | 0.00 | 0.03 | 0.04 | 0.52 | 0.06 | 0.04 | 0.06 | 0.12 | 42.27 | 0.00 |
| K ₂ O | 1.64 | 0.04 | 0.03 | 0.00 | 0.06 | 0.17 | 0.00 | 0.04 | 0.27 | 0.18 | 0.04 |
| P ₂ O ₅ | 0.07 | 0.01 | 0.02 | 0.02 | 0.09 | 0.03 | 0.02 | 0.02 | 0.12 | 0.02 | 0.06 |
| SO ₃ | 0.12 | 0.24 | 53.58 | 56.78 | 0.06 | 0.09 | 70.44 | 0.00 | 0.07 | 55.14 | 0.07 |
| Total | 100.00 | 99.39 | 99.13 | 99.65 | 99.91 | 99.55 | 100.30 | 99.40 | 99.25 | 100.53 | 100.23 |
| LOI | 7.19 | 0.68 | 20.64 | 20.87 | 9.79 | 21.70 | 47.52 | 30.55 | 46.11 | 0.74 | 14.20 |
| FeO | 0.82 | 0.24 | 0.00 | 0.00 | 0.65 | 0.79 | 0.01 | 0.79 | 1.21 | 0.00 | 0.48 |
| Fe ₂ O ₃ | 2.67 | 0.15 | 0.00 | 0.00 | 34.15 | 0.85 | 0.03 | 4.37 | -0.78 | 0.00 | 0.62 |
| Sr | 208 | 1195 | 5491 | 1930 | 112 | 433 | 44 | 103 | 666 | 36 | 86 |
| Zr | 155 | 48 | 146 | 58 | 70 | 359 | 32 | 76 | 102 | 31 | 266 |
| V | 282 | 4 | 7 | 11 | 220 | 83 | < 1 | 54 | 44 | 22 | 136 |
| Cr | 96 | 18 | 5 | 6 | 68 | 47 | 12 | 1195 | 15 | 13 | 142 |
| Ni | 25 | 20 | 1 | 1 | 13 | 2 | 2 | 1479 | 2 | < 2 | 5 |
| Co | 4 | 27 | 22 | 13 | < 1 | < 1 | 20 | 24 | < 1 | < 2 | < 1 |
| <i>Mars hydrothermal</i> | | | | | | | | | | | |
| | ASB003 | ASB230 | ASB601 | ASB902 | ICE003 | SIL304 | NS-103 | GYP316 | | | |
| SiO ₂ | 40.48 | 37.80 | 45.66 | 44.41 | 98.97 | 96.15 | 52.56 | 63.01 | | | |
| TiO ₂ | 0.02 | 0.01 | 0.02 | 0.02 | 0.03 | 0.51 | 1.33 | 0.41 | | | |
| Al ₂ O ₃ | 0.52 | 0.33 | 0.51 | 0.97 | 0.26 | 2.28 | 14.59 | 17.88 | | | |
| Fe ₂ O ₃ T | 11.43 | 17.64 | 6.08 | 6.54 | 0.12 | 0.22 | 12.61 | 4.30 | | | |
| MnO | 0.15 | 0.14 | 0.08 | 0.17 | 0.00 | 0.01 | 0.17 | 0.03 | | | |
| MgO | 45.41 | 44.05 | 46.27 | 35.79 | 0.03 | 0.02 | 6.38 | 2.28 | | | |
| CaO | 0.50 | 0.07 | 0.05 | 10.54 | 0.17 | 0.23 | 9.26 | 3.19 | | | |
| Na ₂ O | 0.08 | 0.07 | 0.05 | 0.06 | 0.06 | 0.05 | 2.41 | 3.82 | | | |
| K ₂ O | 0.01 | 0.00 | 0.00 | 0.00 | 0.05 | 0.22 | 0.68 | 4.81 | | | |
| P ₂ O ₅ | 0.01 | 0.01 | 0.01 | 0.01 | 0.01 | 0.02 | 0.16 | 0.23 | | | |
| SO ₃ | 0.00 | 0.06 | 0.00 | 0.21 | 0.00 | 0.00 | 0.06 | 0.07 | | | |
| Total | 98.61 | 100.18 | 98.73 | 98.72 | 99.69 | 99.71 | 100.21 | 100.03 | | | |
| LOI | 15.87 | 14.72 | 13.32 | 20.92 | 4.71 | 51.66 | 8.12 | 4.04 | | | |
| FeO | 2.22 | 4.15 | 0.33 | 4.22 | 0.13 | 0.18 | 5.61 | 0.19 | | | |
| Fe ₂ O ₃ | 8.96 | 13.03 | 5.71 | 1.85 | 0.02 | 0.02 | 6.38 | 4.09 | | | |
| Sr | 100 | 101 | 18 | 2026 | 8 | 39 | 315 | 676 | | | |
| Zr | 62 | 55 | 14 | 56 | 17 | 353 | 158 | 419 | | | |
| V | 41 | 71 | 41 | 12 | 6 | 29 | 356 | 101 | | | |
| Cr | 6450 | 768 | 2842 | 1025 | 27 | 27 | 175 | 64 | | | |
| Ni | 3980 | 2485 | 3575 | 2013 | < 1 | 22 | 85 | 35 | | | |
| Co | 144 | 117 | 112 | 80 | 15 | 5 | 17 | < 1 | | | |
| <i>Mars low-temperature</i> | | | | | | | | | | | |
| | HAL001 | VER106 | HAW049 | JSC-Mars-1A | HEM105 | CRB131 | CMB9 | PRC001 | PRC003 | NL-110 | NL-116 |
| SiO ₂ | 53.18 | 45.79 | 40.32 | 40.83 | 2.48 | 0.00 | 86.56 | 0.00 | 0.00 | 44.13 | 47.78 |
| TiO ₂ | 0.00 | 1.26 | 3.93 | 3.85 | 0.02 | 0.00 | 0.26 | 0.00 | 0.00 | 0.00 | 0.17 |
| Al ₂ O ₃ | 45.46 | 22.23 | 25.90 | 25.08 | 0.14 | 0.10 | 3.14 | 0.00 | 0.00 | 1.17 | 2.79 |
| Fe ₂ O ₃ T | 0.44 | 9.39 | 15.85 | 16.97 | 96.11 | 0.02 | 4.89 | 0.00 | 0.00 | 9.07 | 10.43 |
| MnO | 0.01 | 0.09 | 0.32 | 0.30 | 0.02 | 0.21 | 0.02 | 0.00 | 0.00 | 0.14 | 0.16 |
| MgO | 0.11 | 13.74 | 3.73 | 2.86 | 0.11 | 0.06 | 1.10 | 0.00 | 0.00 | 43.94 | 36.27 |
| CaO | 0.15 | 1.08 | 4.69 | 5.87 | 0.04 | 98.99 | 2.01 | 0.00 | 0.00 | 0.69 | 0.68 |
| Na ₂ O | 0.07 | 3.60 | 2.38 | 1.97 | 0.19 | 0.06 | 0.62 | 0.00 | 0.00 | 0.07 | 0.31 |
| K ₂ O | 0.05 | 2.64 | 0.59 | 0.42 | 0.01 | 0.01 | 0.31 | 0.00 | 0.00 | 0.01 | 0.35 |
| P ₂ O ₅ | 0.14 | 0.07 | 1.22 | 0.90 | 0.02 | 0.01 | 0.02 | 0.00 | 0.00 | 0.01 | 0.03 |
| SO ₃ | 0.00 | 0.06 | 0.10 | 0.00 | 0.06 | 0.06 | 1.08 | 0.00 | 0.00 | 0.07 | 0.07 |
| Total | 99.61 | 99.95 | 99.03 | 99.05 | 99.20 | 99.52 | 100.01 | 0.00 | 0.00 | 99.30 | 99.04 |
| LOI | 16.31 | 5.29 | 12.99 | 21.60 | 0.40 | 42.67 | 3.24 | 0.00 | 0.00 | 11.84 | 12.24 |
| FeO | 0.00 | 7.06 | 2.77 | 4.45 | 1.35 | 0.01 | 1.25 | 0.00 | 0.00 | 1.47 | 1.97 |
| Fe ₂ O ₃ | 0.44 | 1.54 | 12.77 | 12.02 | 94.61 | 0.01 | 3.50 | 0.00 | 0.00 | 7.44 | 8.24 |
| Sr | 20 | 163 | 1050 | 1088 | 87 | 150 | 21 | 0 | 0 | 110 | 61 |
| Zr | 15 | 442 | 539 | 504 | 50 | 49 | 30 | 0 | 0 | 76 | 93 |
| V | 10 | 264 | 146 | 175 | 93 | 34 | 66 | 0 | 0 | 84 | 60 |
| Cr | 145 | 158 | 50 | 129 | 35 | 15 | 95 | 0 | 0 | 3198 | 3496 |
| Ni | 125 | 54 | 30 | 68 | < 2 | 12 | 35 | 0 | 0 | 4067 | 3270 |
| Co | 2 | 22 | 47 | 39 | < 2 | < 1 | 29 | 0 | 0 | 119 | 105 |
| <i>Mars Igneous</i> | | | | | | | | | | | |
| | HAW006 | HAY020 | ICE170 | OLV003 | PSA004 | GRC007 | MSHhash | | | | |
| SiO ₂ | 50.61 | 59.67 | 46.39 | 40.37 | 51.92 | 63.05 | 61.28 | | | | |

Table 2 (continued)

| | | | | | | | |
|----------------------------------|------------|--------|---------------|---------|------------|--------|--------|
| TiO ₂ | 2.61 | 0.55 | 0.75 | 0.02 | 1.07 | 0.50 | 0.88 |
| Al ₂ O ₃ | 17.45 | 16.08 | 14.36 | 0.11 | 18.29 | 17.14 | 17.13 |
| Fe ₂ O ₃ T | 11.52 | 4.58 | 10.96 | 10.20 | 9.64 | 5.05 | 6.56 |
| MnO | 0.22 | 0.10 | 0.17 | 0.15 | 0.20 | 0.14 | 0.11 |
| MgO | 3.84 | 3.66 | 12.97 | 48.95 | 5.08 | 2.79 | 2.61 |
| CaO | 6.63 | 4.72 | 13.39 | 0.16 | 10.43 | 6.27 | 5.40 |
| Na ₂ O | 4.27 | 6.48 | 1.35 | 0.08 | 3.25 | 3.33 | 4.26 |
| K ₂ O | 1.94 | 3.25 | 0.02 | 0.00 | 0.45 | 1.94 | 1.18 |
| P ₂ O ₅ | 0.91 | 0.30 | 0.03 | 0.00 | 0.16 | 0.11 | 0.19 |
| SO ₃ | 0 | 0.00 | 0 | 0.00 | 0.07 | 0.05 | 0.06 |
| Total | 100 | 99.39 | 100.39 | 100.04 | 100.56 | 100.37 | 99.66 |
| LOI | 1.04 | 3.95 | 0.68 | 0.80 | 4.96 | 1.67 | 1.54 |
| FeO | 5.58 | 0.21 | 8.39 | 8.83 | 3.05 | 3.43 | 3.71 |
| Fe ₂ O ₃ | 5.32 | 4.35 | 1.64 | 0.39 | 6.25 | 1.24 | 2.44 |
| Sr | 1249 | 316.00 | 113 | 29.00 | 312.00 | 332.00 | 516.00 |
| Zr | 449 | 163.00 | 26 | 22.00 | 122.00 | 178.00 | 141.00 |
| V | 106 | 60.00 | 259 | 2.00 | 185.00 | 149.00 | 132.00 |
| Cr | 8 | 145.00 | 953 | 412.00 | 337.00 | 64.00 | 45.00 |
| Ni | 35 | 75 | 710 | 3350 | 65 | 20 | 9 |
| Co | 29 | 38 | 73 | 155 | 58 | < 1 | 2 |
| <i>Lunar basaltic</i> | | | | | | | |
| | SA-20 | MAI203 | FJS-1 | BAS600 | PSA003 | HAW063 | |
| SiO ₂ | 51.71 | 4.64 | 49.19 | 42.63 | 46.21 | 49.86 | |
| TiO ₂ | 2.91 | 45.05 | 1.51 | 6.56 | 1.68 | 2.44 | |
| Al ₂ O ₃ | 14.69 | 2.76 | 16.90 | 11.75 | 15.78 | 13.16 | |
| Fe ₂ O ₃ T | 13.21 | 42.47 | 12.79 | 18.09 | 11.92 | 12.64 | |
| MnO | 0.18 | 0.13 | 0.20 | 0.22 | 0.19 | 0.18 | |
| MgO | 3.44 | 2.14 | 5.70 | 5.88 | 9.10 | 8.29 | |
| CaO | 9.62 | 1.02 | 9.75 | 11.36 | 10.38 | 10.65 | |
| Na ₂ O | 2.76 | 0.39 | 2.67 | 2.38 | 3.07 | 2.24 | |
| K ₂ O | 1.09 | 0.15 | 0.71 | 0.29 | 0.76 | 0.44 | |
| P ₂ O ₅ | 0.62 | 0.10 | 0.30 | 0.08 | 0.68 | 0.26 | |
| SO ₃ | 0.00 | 0.10 | 0.06 | 0.07 | 0.06 | 0.06 | |
| Total | 100.23 | 99.22 | 99.78 | 99.31 | 99.83 | 100.22 | |
| LOI | 2.67 | 0.40 | 4.76 | 0.91 | 0.63 | 1.85 | |
| FeO | 6.01 | 26.78 | 7.75 | 5.60 | 7.74 | 6.77 | |
| Fe ₂ O ₃ | 6.53 | 12.71 | 4.18 | 11.87 | 3.32 | 5.12 | |
| Sr | 348 | 46 | 374 | 188 | 865 | 395 | |
| Zr | 183 | 209 | 107 | 72 | 168 | 183 | |
| V | 441 | 1560 | 414 | 735 | 237 | 347 | |
| Cr | 90 | 495 | 147 | 45 | 212 | 479 | |
| Ni | 75 | 210 | 56 | 75 | 3 | 149 | |
| Co | 43 | 90 | 25 | 44 | 29 | 33 | |
| <i>Lunar anorthositic</i> | | | | | | | |
| | MAI001 | PSA001 | TBD – Anorth. | CHX009c | Shimizu-HS | | |
| SiO ₂ | 45.85 | 47.50 | 42.99 | 57.79 | 54.01 | | |
| TiO ₂ | 3.12 | 0.06 | 0.01 | 0.11 | 0.65 | | |
| Al ₂ O ₃ | 16.92 | 31.69 | 32.74 | 26.26 | 18.06 | | |
| Fe ₂ O ₃ T | 14.44 | 1.73 | 0.81 | 0.35 | 10.05 | | |
| MnO | 0.14 | 0.02 | 0.02 | 0.01 | 0.17 | | |
| MgO | 2.95 | 0.72 | 0.58 | 0.14 | 3.58 | | |
| CaO | 10.56 | 15.99 | 21.88 | 8.01 | 9.95 | | |
| Na ₂ O | 3.67 | 2.35 | 0.91 | 6.38 | 2.21 | | |
| K ₂ O | 0.68 | 0.04 | 0.06 | 0.89 | 0.71 | | |
| P ₂ O ₅ | 2.01 | 0.02 | 0.02 | 0.03 | 0.10 | | |
| SO ₃ | 0.00 | 0.12 | 0.10 | 0.06 | 0.05 | | |
| Total | 100.34 | 100.24 | 100.12 | 100.03 | 99.54 | | |
| LOI | 0.89 | 0.42 | 1.10 | 0.43 | 0.74 | | |
| FeO | 7.66 | 1.41 | 0.51 | 0.20 | 6.16 | | |
| Fe ₂ O ₃ | 5.93 | 0.16 | 0.24 | 0.13 | 3.20 | | |
| Sr | 637 | 207 | 491 | 1383 | 325 | | |
| Zr | 82 | 173 | 60 | 93 | 68 | | |
| V | 192 | 29 | 37 | 31 | 271 | | |
| Cr | 31 | 15 | 40 | 60 | 215 | | |
| Ni | 25 | 5 | < 2 | 10 | 59 | | |
| Co | 22 | < 1 | < 1 | < 1 | 20 | | |
| <i>Impactite</i> | | | | | | | |
| | HMP-05-026 | CM065 | W05-41 | STM030 | STM003 | STM889 | |
| SiO ₂ | 19.89 | 56.44 | 55.52 | 72.05 | 63.01 | 66.01 | |
| TiO ₂ | 0.10 | 0.75 | 0.39 | 0.41 | 0.55 | 0.39 | |
| Al ₂ O ₃ | 2.97 | 22.33 | 26.84 | 14.52 | 16.35 | 16.70 | |
| Fe ₂ O ₃ T | 1.17 | 5.05 | 1.53 | 2.49 | 6.46 | 3.52 | |
| MnO | 0.02 | 0.08 | 0.04 | 0.05 | 0.08 | 0.06 | |

Table 2 (continued)

| | | | | | | |
|--------------------------------|-------|--------|--------|--------|--------|-------|
| MgO | 15.84 | 1.44 | 0.40 | 0.71 | 2.67 | 3.20 |
| CaO | 58.66 | 7.92 | 9.60 | 1.90 | 3.74 | 2.52 |
| Na ₂ O | 0.12 | 4.44 | 4.79 | 4.05 | 3.31 | 3.22 |
| K ₂ O | 0.59 | 1.49 | 0.71 | 3.76 | 3.64 | 3.91 |
| P ₂ O ₅ | 0.04 | 0.27 | 0.08 | 0.13 | 0.19 | 0.14 |
| SO ₃ | 0.29 | 0.07 | 0.40 | 0.07 | 0.06 | 0.07 |
| Total | 99.69 | 100.28 | 100.30 | 100.14 | 100.06 | 99.74 |
| LOI | 37.20 | 1.35 | 2.59 | 0.67 | 3.18 | 6.11 |
| FeO | 0.19 | 2.32 | 0.31 | 0.93 | 0.36 | 0.25 |
| Fe ₂ O ₃ | 0.96 | 2.47 | 1.19 | 1.46 | 6.06 | 3.24 |
| Sr | 523 | 676 | 830 | 369 | 652 | 525 |
| Zr | 90 | 242 | 92 | 358 | 200 | 204 |
| V | 42 | 87 | 17 | 69 | 149 | 100 |
| Cr | 17 | 94 | < 2 | 87 | 110 | 79 |
| Ni | 15 | 15 | 15 | 13 | 25 | 18 |
| Co | < 1 | < 1 | 8 | < 1 | < 1 | 3 |

with a resolution of 640 × 480 voxels. Imaging of the full sample volume was accomplished by putting the samples on a rotating turntable and repositioning them along their three major rotation axes so that all surfaces could be imaged. Typically, 54 individual images were collected for each sample.

After imaging, the point clouds were imported into the Polyworks visualisation software tool (Innovmetric Inc., Quebec City, Canada). The software fits a mesh of triangles to the surface outlined by the point cloud. A human operator can then proceed to assemble multiple meshes into a closed 3D model following the method described in [Smith et al. \(2006\)](#). During this process, the edges around each individual image were trimmed as they can be distorted by field-of-view curvature, causing tiny surficial protrusions on the model. Surfaces exhibiting an unrealistic stretched texture from being imaged at grazing incidence were also eliminated. Following the manual editing steps, the software automatically eliminated redundant data, and merged the meshes together so that the model was covered by a single surface. Finally, the model was manually corrected to fill any persistent holes and remove unphysical irregularities. Because a high level of user intervention and correction is required, the 3D reconstructions contain a subjective or user-dependent element, which cannot be entirely removed at this time.

2.16. Sample photography and microimaging

Images of each sample were captured at various orientations using a Nikon D90 digital single-lens reflex camera with a Nikkor 18–105 mm lens. Microscopic images of natural rock surfaces were acquired using a Pentax Optio with a focal length of 1 cm.

3. Results

All analytical results are reported for each sample in the supplemental materials. In this section, the essential mineral and chemical features of the samples are summarized in tabular form. [Table 1](#) gives the provenance and major mineralogical and (where appropriate and relevant) textural features of each sample. [Table 2](#) summarizes the bulk geochemical data for each sample, with major elements in units of oxide weight percent, and trace elements in units of ppm by weight. Note that in [Table 2](#), iron is listed as Fe₂O₃T (total) among the major elements, but the FeO and Fe₂O₃ contents have been measured and are listed immediately below the major elements.

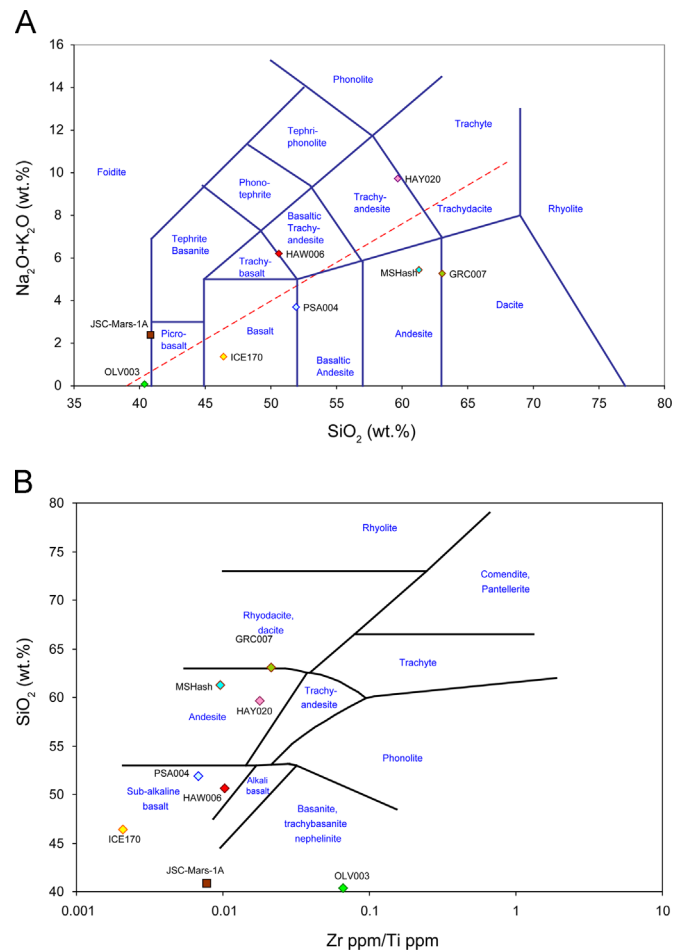


Fig. 1. Geochemical discrimination diagrams for Mars igneous rocks and JSC-Mars-1 palagonitic soil simulant (derived from basaltic eruptives from Hawai'i). (A) Total alkalis vs. silica diagram ([Le Bas et al., 1986](#)), contrasted (B) with the SiO₂ vs. Zr/Ti diagram of [Winchester and Floyd \(1977\)](#). Unweathered samples (ICE170, HAW006, MSHash, GRC007) are generally well-classified by both diagrams, but weathered materials (PSA004, HAY020), reworked and weathered (JSC-Mars-1) and a plutonic material (OLV003) are not consistently classified.

4. Discussion

The volume of data collected in this study precludes a detailed discussion of every sample. Here, we present a few chosen case studies to highlight some of the unique and interesting features of the CSA analogue materials suite and associated data.

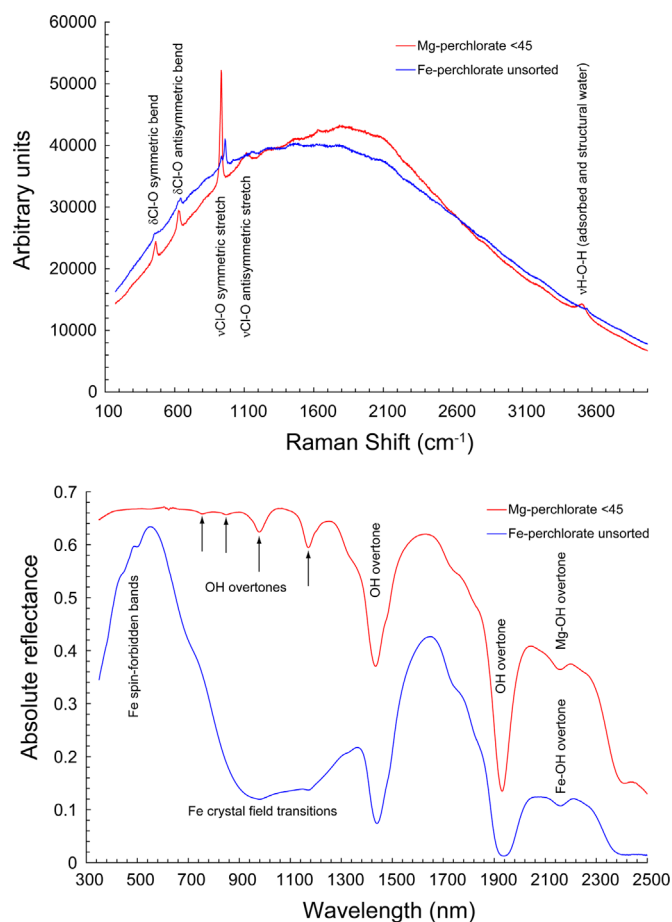


Fig. 2. (A) Raman (532 nm excitation) and (B) ultraviolet–visible–near infrared (UV–vis–NIR, 350–2500 nm) reflectance spectra of iron and magnesium perchlorates (samples PRC001 and PRC003). The Fe perchlorate ‘unsorted’ spectra are shown owing to the near-impossibility of sieving this material, as it is highly hydroscopic and rapidly forms clumps and aggregates. In reflectance, both phases show strong O–H vibration and combination bands due to structural water. In the Fe-perchlorate, Fe²⁺ produces a strong crystal field band centred near ~1000 nm.

4.1. Rock type discrimination using bulk geochemistry

Because it is relatively straightforward to measure the major element composition of rocks using rover/lander instruments, geochemical discrimination diagrams constructed from major element concentrations are widely used in the interpretation of rover data. Fig. 1A shows the commonly used total alkali vs. silica (TAS) diagram of Le Bas et al. (1986) for the martian igneous analogue materials suite and the JSC-Mars-1 palagonitic soil simulant. A danger in the use of the TAS diagram is that physical (e.g., sorting during transport) and chemical processes (e.g., weathering, hydrothermal alteration) can greatly affect the major element concentrations used in constructing this diagram. Fig. 1B shows an alternative discrimination diagram based on SiO₂ and the generally immobile elements Zr and Ti (Winchester and Floyd, 1977). To illustrate the relative displacements inherent in using the two different classification schemes for weathered igneous samples, Fig. 1A and B shows how some of the weathered samples suggest different classifications depending on the particular compositional diagram that is used. Caution must be exercised in drawing petrogenetic conclusions or making inferences regarding martian geological processes using the TAS diagram.

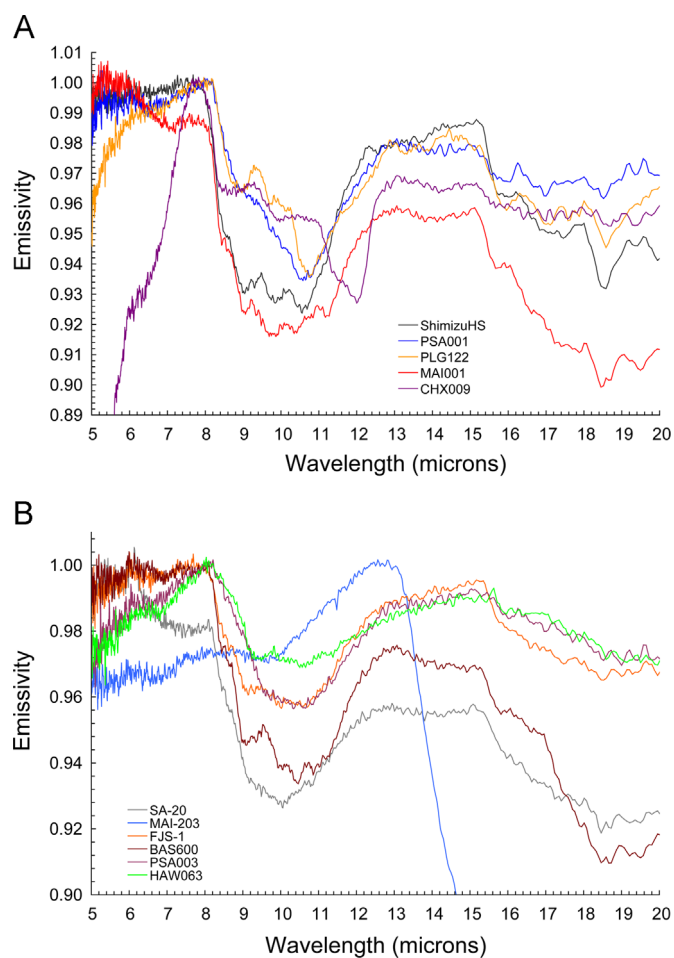


Fig. 3. Emissivity spectra of lunar analogue materials. (A) Lunar highlands (anorthositic) materials. (B) Mare (basaltic) materials. The positions of the Christiansen features (CFs) broadly correlate with silicate mineralogy, in particular, the wavelength of the CFs increases in plagioclase-dominant anorthositic materials versus mafic basaltic materials. It is also notable that the Christiansen feature of ilmenite (MAI-203) is at much lower energy (longer wavelength) than any silicates.

4.2. Example 2: Spectroscopy of perchlorate compounds

Perchlorate compounds are anions of high interest in Mars exploration, as their presence in the near surface may in part account for the non-detection of organic compounds (perchlorate may oxidise and destroy any organics, even those introduced by carbonaceous meteorite infall) in multiple lander and rover experiments. Perchlorate may also be an important component of near-surface brines (Gough et al., 2011), and play a role in the martian chlorine geochemical cycle. Even more speculatively, it is possible for some microbes to use perchlorate as an oxidant in metabolic reactions. Fig. 2 presents 532 nm excitation Raman and UV–vis–NIR reflectance spectra of two perchlorates, Mg-perchlorate and Fe(II)-perchlorate. The perchlorate compounds were purchased as Mg(ClO₄)₂ and Fe(ClO₄)₂·6H₂O, however, XRD indicates that the Mg-perchlorate has hydrated and includes the hexahydrate and possibly other hydration states (2 and 4 hydrate phases are also known to exist). This is advantageous, as investigations by Robertson and Bish (2011) have demonstrated that the most likely perchlorate phase near the martian surface is the Mg-perchlorate hexahydrate. Fe(II)-perchlorate is also sensitive to oxidation and photo-oxidation processes, which may lead to the formation of Fe³⁺ cations. The vibrational features related to the perchlorate anion may enable future Raman instruments (e.g.,

instruments planned for ExoMars and proposed for MSL 2020) to detect perchlorate in martian soils.

4.3. Example 3: Thermal infrared emission spectra of lunar analogues

Thermal emission data from the Lunar Reconnaissance Orbiter (LRO) Diviner instrument have been used to estimate the bulk mineralogy of the lunar surface (Greenhagen et al., 2010). Fig. 3 shows thermal emission spectra of lunar analogue materials for the highlands (anorthositic) and mare (basaltic) suites. It has been shown that the effects of vacuum and the nature of lunar regolith greatly reduce the spectral contrast of lunar materials, which has led to the use of the wavelength position of the principal Christiansen feature (CF) for the evaluation of lunar surface mineralogy (Logan et al., 1978; Nash et al., 1993; Greenhagen et al., 2010). In particular, the energy of the CF generally increases with increasing polymerisation of the silicate network, for example, plagioclase or quartz have shorter wavelength CFs than pyroxene or olivine (Logan et al., 1978; Glotch et al., 2010; Greenhagen et al., 2010; Song et al., 2013). The position of the principal Christiansen feature is relatively insensitive to grain size and other physical effects, but can be strongly affected by experimental and observational effects, for example, by changing the thermal structure of the optically active layer of a powder in vacuum compared to the same powder in air, and therefore use of the CF must be approached cautiously (e.g., Logan et al., 1978). It is also notable that the emissivity maximum of ilmenite (MAI-203) is at much lower energy (longer wavelength) than any silicates, due to the much lower energy of the Fe–O and Ti–O stretching fundamental vibrations versus comparable Si–O and Al–O fundamentals. Ideally, emission spectra of lunar analogue materials should be collected under lunar-like conditions of vacuum and temperature. The measurements reported here serve as a baseline for other spectra collected under different conditions. The spectra of the 45–1000 μm size fractions collected under ambient conditions are especially likely to be very

close to those acquired under lunar conditions, as strong thermal gradients do not develop in the optically active layer of coarse particulates. For comparison to lunar spectra, the finely particulate size fraction ($< 45 \mu\text{m}$) spectra of each sample would need to be collected in a simulated lunar environment (e.g., Donaldson Hanna et al., 2012a,b; Shirley and Glotch, 2015).

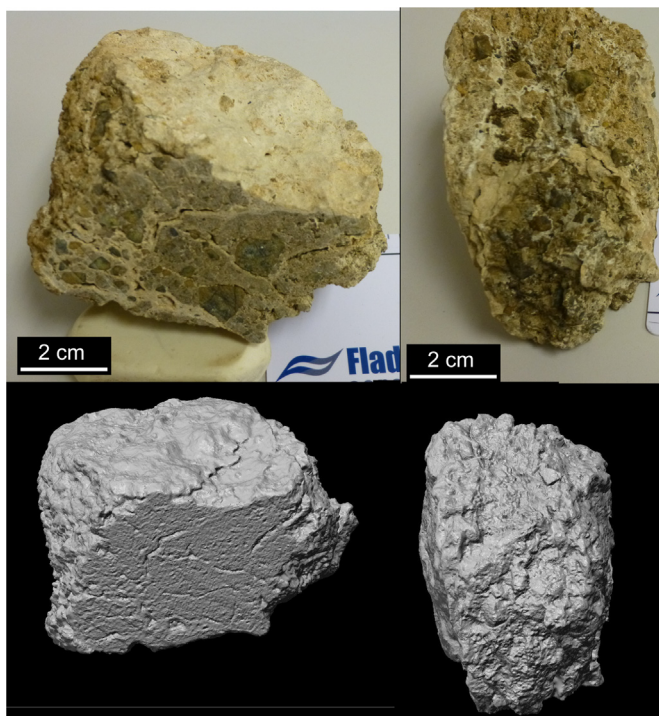


Fig. 4. Example of 3D imaging. Top row: conventional photographs of sample NL 105 from two different viewpoints; bottom row: The corresponding 3D model built from laser images of the sample and can be viewed from any viewpoint.

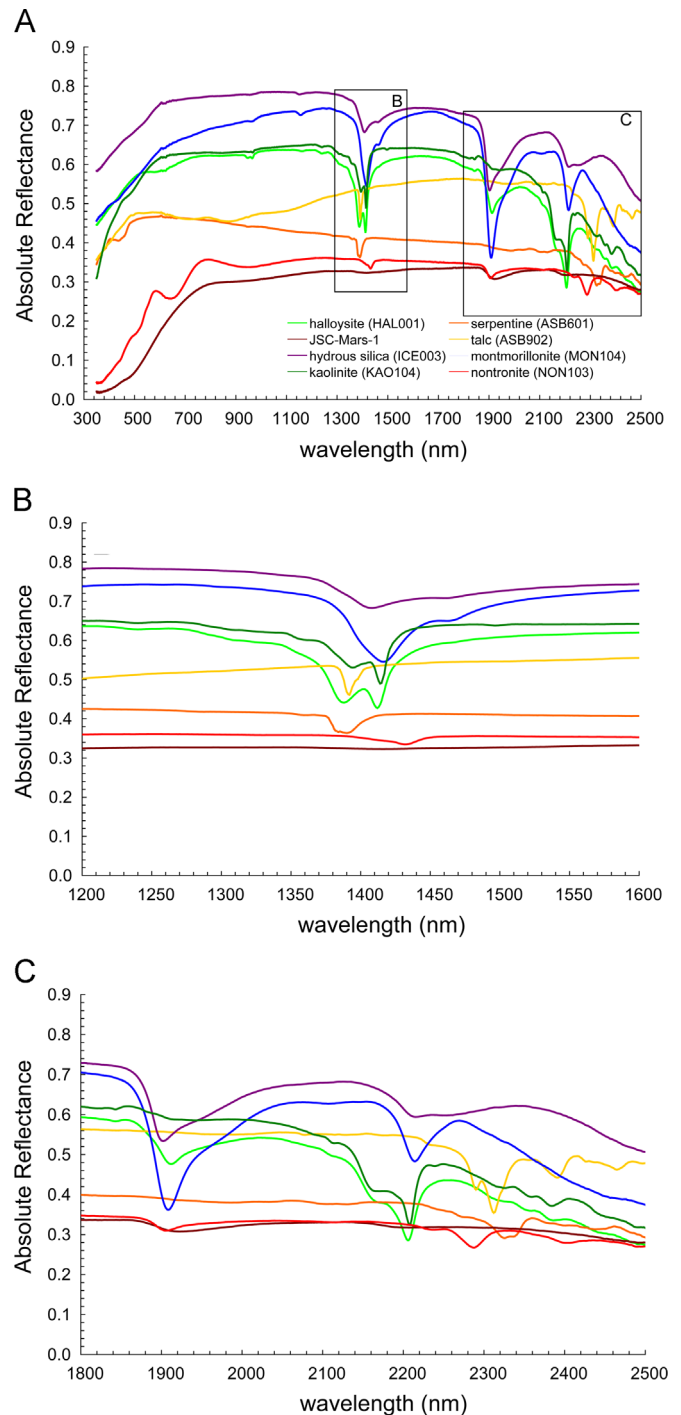


Fig. 5. (A) Example reflectance spectra of Mars analogue phyllosilicates, hydrous silica, and palagonitic soil simulant JSC-Mars-1. (B) Detail of the region near ~ 1400 nm containing spectral features due to OH stretching overtones. (C) Detail of the region between 1800 and 2500 nm containing spectral features due to metal–OH combinations and overtones. This figure also highlights some potential ambiguities in the interpretation of remote sensing data. For example, the positions of the strongest features of hydrous silica and montmorillonite are very similar and could easily be confused in noisy or low spectral resolution data.

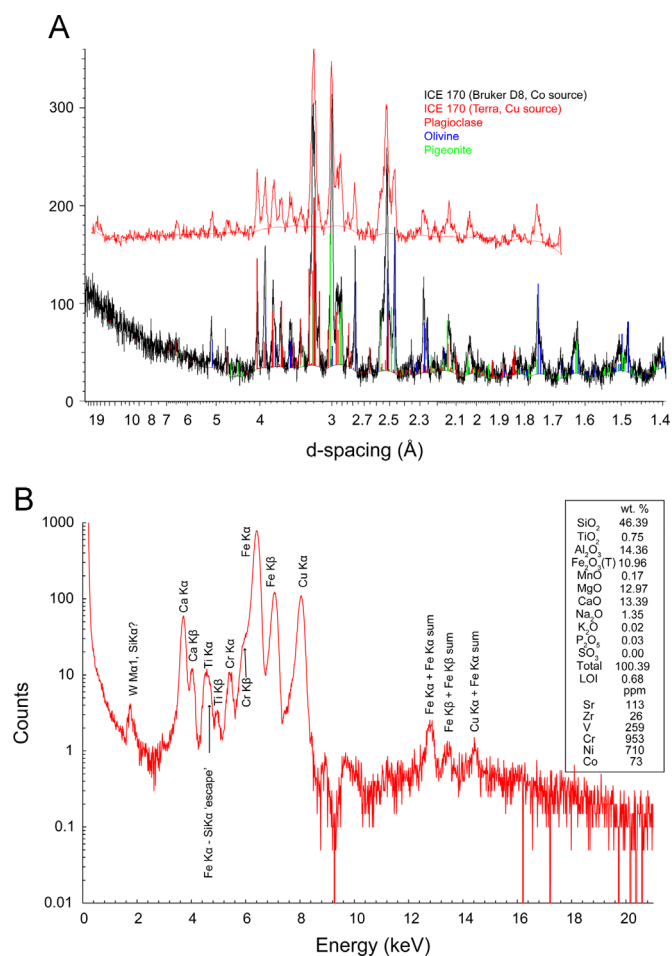


Fig. 6. Comparison of field-portable and laboratory X-ray diffraction (A) and X-ray fluorescence (B) data for Icelandic basalt ICE-170. Data from both XRD instruments show the major peaks of plagioclase (bytownite), forsteritic olivine, and pigeonite. The Bragg angles for laboratory Bruker D8 data (Co source) and field-portable Terra instrument (Cu source) have been transformed to D-spacing in Angstroms using Bragg's law. The Terra XRD data are vertically offset by +150 counts for clarity. Field portable XRF data show clear evidence only for Fe, Cr, Ti, and Ca. Laboratory XRF analysis confirms and quantifies these elements, and reveals the presence and concentrations of several more (box in B). The chemical and crystal-structural data from the field portable XRD/XRF instrument would allow a reasonable first-order assessment of the sample as a basaltic rock, with the presence of Cr being suggestive of the presence of Cr-bearing phase. In this case, XRD did not reveal the identity of the Cr-bearing phase, but optical microscopy and EPMA analysis indicates the presence of chromite.

4.4. 3D imaging of whole-rock samples

Fig. 4 shows an example of three-dimensional sample imaging. The volumetric model can be used to record the positions of point analyses and sub-samples for archival purposes.

4.5. Reflectance spectra of hydroxyl-bearing Mars analogue materials

The identification of phyllosilicates, hydrous silica, and other hydrous phases on the martian surface has important implications for the geological history of the host lithologies. The CSA analogue materials suite includes numerous mineral and rock samples similar to those identified using orbital hyperspectral data. The key features used for identification, characterization and mapping of hydrous phases are OH and metal-OH (dominantly Fe-OH, Mg-OH, Al-OH, and Si-OH) overtone and combination absorptions, the

strongest of which are located near ~ 1400 nm, ~ 1900 nm and ~ 2100 – 2400 nm. The metal-OH stretching and combination features have been used to identify phyllosilicates and hydrous silicates in hyperspectral data from the Compact Reconnaissance Imaging Spectrometer for Mars (CRISM) instrument on Mars Reconnaissance Orbiter (MRO) (Wray et al., 2008; McKeown et al., 2009). Fig. 5 shows the spectra of selected hydroxylated minerals similar to those inferred to be present on Mars, including Al-OH bearing kaolinite (KAO104), halloysite (HAL001), Mg-OH bearing serpentine (ASB601), montmorillonite (MON104) and talc (ASB902), Fe-OH bearing nontronite (NON103), Si-OH bearing hydrous silica (ICE003), and the NASA JSC-Mars-1 palagonitic soil Mars regolith simulant.

4.6. Example 1: Comparison of laboratory and field-portable X-ray diffraction and fluorescence

Fig. 6 presents a comparison of laboratory mineral identification data by XRD and chemical analysis by XRF, with data acquired with the field-portable XRD–XRF instrument comparable to the CheMin instrument deployed on MSL. The diffractograms for both the laboratory Bruker D8 diffractometer and the Terra portable XRD/XRF instrument show characteristic reflections for the minerals plagioclase (bytownite), forsteritic olivine, and pigeonite. X-ray fluorescence from the Terra instrument reveals the presence of Fe, Ca, Ti, and Cr. Laboratory XRF analysis confirms the presence of these elements, but also reveals many others that the field instrument did not detect. It is notable that neither lab nor field-portable instrumentation has detected diffraction peaks for chromite in this sample, though it is observed in thin section using reflected light or electron-beam microanalysis. Laboratory XRF shows that the sample contains 953 ppm Cr.

4.7. Fidelity and limitations of analogue materials

There are some issues which are difficult to address adequately for lunar analogue materials that are related to the very low activities of O₂, H₂O and other volatile, reactive species in the lunar crust and interior. Despite recent discoveries of hydration (a mixture of adsorbed and structural hydroxyl, interstitially hosted hydrogen, and adsorbed molecular water) in lunar samples (e.g., Pieters et al., 2009; Sunshine et al., 2009; McCord et al., 2011; Hui et al., 2013; Saal et al., 2013), the lunar surface and interior remain extremely volatile-poor compared to Earth (or Mars). The situation is similar for fO₂, as lunar samples are almost entirely free of Fe³⁺. Therefore, the use of any techniques intended to measure (or to be strongly affected by) hydration or the presence of oxidised Fe³⁺ (or other multivalent cations) must be approached with caution. Variability in oxygen fugacity can be recognised in the fact that all the lunar analogue samples have a detectable Fe₂O₃ content. Another example is microimaging of terrestrial ilmenite (sample MAI203) which reveals a fine lamellar exsolution microstructure of haematite within the ilmenite host. The effect is also seen in the presence of phases such as mica and amphibole that are extremely rare or absent from known lunar rocks incorporated in some of the lunar simulants.

Planetary trends in geochemistry cannot easily be replicated using naturally-occurring terrestrial materials. For example, the Fe–Mg–Mn systematics of basalts have been shown to be unique for each of Earth, the Moon, Mars, and Vesta (Papike et al., 2003), and the basaltic samples in the CSA analogue suite will follow the Earth trends for these elements. Similarly, isotopic and chemical composition signatures of planetary parentage will reflect the terrestrial origin of all the samples in the CSA planetary analogue materials suite.

5. Conclusions

The terrestrial materials characterized in this study were chosen to be representative analogues for some materials known or suspected to be present on the surfaces of Mars and the Moon. The samples have been chosen to represent a broad range in terms of major mineral and amorphous phases present, assemblages and textures of minerals, and in most bulk chemical properties. The lunar analogues were chosen to represent the broad division of the lunar surface into anorthosite-dominant highlands and basaltic mare. Conversely, the martian analogues were chosen largely to represent materials suspected to be present based on remotely sensed data but unknown in martian meteorites, with the exception of some of the Mars analogue igneous samples. It is hoped that the CSA analogue materials suite will be complementary to other analogue material libraries (e.g., ISAR), for example by extending the range of Mars analogue materials to include additional sedimentary, low-temperature and hydrothermal assemblages. Many of the analytical techniques used in this study are similar to those that are being (or will be) applied in robotic planetary exploration missions (e.g., LIBS, Raman spectroscopy, portable XRD/XRF, reflectance spectroscopy and induced fluorescence). Because the materials described here are available in much larger quantities than their extraterrestrial analogues (and, in some cases such as Mars sediments, no extraterrestrial (meteorite) examples are known), this analogue material library can help mature a variety of scientific and technological investigations. Flight instrument characterization and calibration will continue to

rely on tests using bona fide extraterrestrial materials (meteorites, sample returns), but experiments using analogue materials may enable the best use of such rare and valuable samples.

Acknowledgements

The University of Winnipeg's HOSERLab was established with funding from the Canada Foundation for Innovation, the Manitoba Research Innovations Fund and the Canadian Space Agency, whose support is gratefully acknowledged. This study was supported by research grants from NSERC, the Canadian Space Agency and the University of Winnipeg. Thanks to Nicolas Bost and an anonymous reviewer for many helpful comments and suggestions that led to substantial improvements to this manuscript. MRMI gratefully acknowledges funding from the NSERC CREATE Canadian Astrobiology Training Program and the Mineralogical Association of Canada. This work was undertaken in response to CSA Solicitation 9F052-130356/A: Analogue Geological Spectral Library. Thanks to Dr. Andrew Locock (University of Alberta) for assistance with EPMA measurements and Jeffrey A. Berger for very helpful discussions. The geochemical discrimination diagrams were plotted using modifications of spreadsheets provided by Dr. Kurt Hollöcher, Dept. Geology, Union College (http://minerva.union.edu/holloch/c_petrology/discrim/discrim.htm), and we are thankful to him for posting them "for the benefit of all humanity".

Appendix A. Analytical data for all samples are provided as a digital appendix to this paper

A single spreadsheet file contains data for each subset of samples (Mars sedimentary, Mars analogue hydrothermal, Mars analogue low-temperature, Mars analogue igneous, Lunar analogue basaltic, Lunar analogue anorthositic, and Impactite). Within the corresponding spreadsheet file, a single page contains all analytical data for a particular sample.

Each spreadsheet has been laid out in the same manner as follows:

| | |
|-------------------------|----------------------------------------------------------------------------------------------------------------------------------------------------------------------------------------------------------------------------------------------------------------------------------------------------------------------------------------------------------------------------------------------------------------------------------------------------------------------------------------------------------------------------|
| Column A: | Sample ID, example photographic image, XRD Rietveld output (phases detected and abundances from X-ray diffractograms), and petrographic notes |
| Columns C&D: | Powder X-ray diffractogram from Bruker D8 Advance on < 45 µm samples. Column C: two-theta angle; column D: intensity (arbitrary counts) |
| Columns F&G: | X-ray fluorescence elemental abundances (as oxides for major elements) in weight%. Total is expressed on a loss on ignition (LOI; i.e., volatiles-free basis), and all Fe reported as Fe ₂ O ₃ . LOI=loss on ignition (weight loss after heating sample in air at 950 °C for one hour). |
| Columns I&J: | Trace element contents from XRF analysis in parts per million (ppm). Column I: element; column J: abundance in parts per million. |
| Columns L&M: | Fe ²⁺ (as FeO) and Fe ³⁺ (as Fe ₂ O ₃) from wet chemistry titration, expressed in weight%. |
| Columns O&P: | Powder X-ray diffractogram of < 45 µm size powder using Terra portable XRD/XRF instrument. Column O: two-theta angle; column P: intensity (arbitrary counts). |
| Columns R&S: | X-ray fluorescence spectrum using Terra portable XRD/XRF instrument. Column R: photon energy; column R: intensity (arbitrary units). |
| Columns U-Y: | UV reflectance (from 198 to 400 nm, measured at incidence angle (<i>i</i>) and emission angle (<i>e</i>) of 0°) measured using Maya spectrometer on < 45 µm powder, 45–1000 µm powder, and whole rock or unsorted powders; graphs included. Column U: wavelength values; column V: reflectance of < 45 µm size powder (in percent); column W: reflectance of 45–1000 µm size sample (in percent); column X: reflectance of unsorted powder or whole rock surface (in percent); column Y: graph of reflectance spectra. |
| Columns AA-AE: | Visible-near infrared reflectance (from 400 to 1100 nm, measured at incidence angle (<i>i</i>) of 30° and emission angle (<i>e</i>) of 0°) using Maya spectrometer on < 45 µm powder, 45–1000 µm powder, and whole rock or unsorted powders; graphs included. Column AA: wavelength values; column AB: reflectance of < 45 µm size powder; column AC: reflectance of 45–1000 µm size sample; column AD: reflectance of unsorted powder or whole rock surface; column AE: graph of reflectance spectra. |
| Columns AF-AJ: | Ultraviolet-visible-near infrared reflectance (from 350 to 2500 nm, measured at incidence angle (<i>i</i>) of 30° and emission angle (<i>e</i>) of 0°) using ASD spectrometer on < 45 µm, 45–1000 µm and whole rock or unsorted powders; |

graphs included. Column AF: wavelength values; column AG: reflectance of < 45 μm size powder (absolute reflectance); column AH: reflectance of 45–1000 μm size sample (absolute reflectance); column AI: reflectance of unsorted powder or whole rock surface (absolute reflectance); column AJ: graph of reflectance spectra.

Columns AK-AO: Mid-infrared reflectance (from 1.96 to 5.0 μm , measured at incidence angle (i) of 30° and emission angle (e) of 0°) using D&P model 102 F portable Fourier Transform Infrared (FTIR) spectrometer on < 45 μm powder, 45–1000 μm powder, and whole rock or unsorted powders; graphs included. Column AK: wavelength values; column AL: reflectance of < 45 μm size powder (absolute reflectance); column AM: reflectance of 45–1000 μm size sample (absolute reflectance); column AN: reflectance of unsorted powder or whole rock surface (absolute reflectance); column AO: graph of reflectance spectra.

Columns AP-AR: Emissivity (from 2000 to 200 cm^{-1}) spectra of 200–1000 μm size powder; plots included. Column AP: wavelength values (in inverse centimeters (cm^{-1})); column AQ: absolute emissivity. Column AR: graph of emissivity spectra.

Columns AS-AV: Raman spectra (175–4000 cm^{-1} using an excitation of 532 nm) on < 45 μm powder and whole rock or unsorted powders; graphs included. Column AS: Raman shift (in inverse centimeters (cm^{-1})); column AT: intensity for < 45 μm size powder (in arbitrary units); column AU: intensity for whole rock or unsorted powder (in arbitrary units). Column AV: graph of Raman spectra.

Columns AW-AY: Ultraviolet-induced fluorescence spectra (from 400 to 1100 nm, measured at an incidence angle (i) and emission angle (e) of 0°) using an excitation of 405 nm on < 45 μm size powders; graphs included. Column AW: wavelength values (in nanometers); column AX: intensity (in arbitrary units); column AY: graph of spectra.

Columns BA-BY: Laser-induced breakdown spectrometer (LIBS) spectra (from 197 to 838 nm) using an excitation of 1564 nm on < 45 μm powders and whole rock; 10 spot spectra acquired for each sample. Column BA: wavelength values; columns BB to BK: 10 individual point spectra for < 45 μm powder; column BL: average of the 10 individual point spectra for < 45 μm powder; columns BN to BW: individual point spectra for whole rock; column BX: average of the 10 individual point spectra for whole rock.

Appendix B. Comparison of ISAR and CSA analogue sample suites and data sets

As of this writing (June 18th, 2015) ISAR includes 45 samples (<http://isar.cnrs-orleans.fr/isar/>) which 15 were given a cursory description in the paper of Bost et al. (2013). The CSA suite includes 53 samples, and there is rather limited overlap within the Mars-analogue samples in each collection. The CSA suite includes many rock types not covered by ISAR, especially low-T weathering and hydrothermal phases, whereas ISAR contains komatiites and synthetic basalts not covered in the CSA collection (cf. Table 1 of this study with Table 2 of Bost et al. (2013) or <http://isar.cnrs-orleans.fr/isar/>). The CSA suite also contains lunar-analogue and impact-affected materials not covered by ISAR. Apart from petrographic and hand-sample images and a few EPMA analyses of major minerals, none of the ISAR data are directly presented in the paper of Bost et al. (2013). We are presenting (as supplementary data due to its size) the entire CSA analogue data set. The techniques applied to the ISAR suite (as reported by Bost et al. 2013) place a strong emphasis on thin section methods; they list (their Table 4): optical image ('macro' and 'micro'), bulk rock Raman spectra, powder XRD, bulk rock infrared reflectance spectra, ^{57}Fe Mössbauer spectroscopy of 'fresh' surfaces, in situ Raman on a thin section, energy-dispersive spectroscopy on thin sections, microprobe analysis of major minerals in thin section, and Raman mapping of thin sections; all are reported in terms of minerals that are 'unambiguous', 'probably', 'ambiguous', 'impossible' to identify. The CSA suite presented here includes optical photographs of the whole rocks, 3D rock imaging, thin section optical images in transmitted (cross- and plane-polarized and reflected light, quantitative mineral analysis using EPMA, bulk rock major and minor element geochemistry by XRF and $\text{Fe}^{3+/2+}$ ratio determination by wet chemistry, ultraviolet reflectance (200–400), UV-vis-NIR (350–2500 nm), visible (400–1100 nm), and infrared reflectance (2.5–5.2 μm) of three grain size fractions (< 45 μm , 45–1000 μm , and > 1000 μm), thermal emission spectra of the 45–1000 μm fraction, ultraviolet fluorescence spectra with 365 nm excitation, powder XRD using both laboratory and field-portable instruments, field-portable XRF, powder Raman spectra, and laser-induced breakdown spectra. Comparing the two data sets, the ISAR suite has ^{57}Fe Mössbauer spectroscopy (sensitive to mineralogy and Fe valance) which the CSA suite does not (though we do present measurements that can give some of the same information, particularly $\text{Fe}^{3+/2+}$ ratio from wet chemistry). Conversely, the spectral measurements in the CSA suite, particularly those in the UV, visible, and near-infrared ranges, as well as the fluorescence spectra, LIBS measurements, and 3D imaging, have no counterpart in the ISAR data set. Reflectance measurements are a key method for remote sensing by orbiting and landed instruments such as MRO CRISM and ChemCam's passive reflectance mode. The ISAR data set also includes no bulk chemical analysis for rock samples.

Appendix C. Supplementary material

Supplementary data associated with this article can be found in the online version at <http://dx.doi.org/10.1016/j.pss.2015.09.001>.

References

- Abbey, S., 1983. Studies in "Standard Samples" of silicate rocks minerals 1962–1982. Geological Survey of Canada Paper, pp. 83–115.
- Abramov, O., Kring, D.A., 2005. Impact-induced hydrothermal activity on early Mars. *J. Geophys. Res.* 110.
- Allen, C.C., Gooding, J.L., Jercinovic, M., Keil, K., 1981. Altered basaltic glass-a terrestrial analog to the soil of Mars. *Icarus* 45, 347–369.
- Arvidson, R.E., Ruff, S.W., Morris, R.V., Ming, D.W., Crumpler, L.S., Yen, A.S., Squyres, S.W., Sullivan, R.J., Bell, J.F., Cabrol, N.A., Clark, B.C., Farrand, W.H., Gellert, R., Greenberger, R., Grant, J.A., Guinness, E.A., Herkenhoff, K.E., Hurowitz, J.A., Johnson, J.R., Klingelhofer, G., Lewis, K.W., Li, R., McCoy, T.J., Moersch, J., McSweeney, H.Y., Murchie, S.L., Schmidt, M., Schroder, C., Wang, A., Wiseman, S., Madsen, M.B., Goetz, W., McLennan, S.M., 2008. Spirit Mars Rover Mission to the Columbia Hills, Gusev Crater: mission overview and selected results from the Cumberland Ridge to Home Plate. *J. Geophys. Res.* 113.
- Baek, et al., 2015. Baseline correction using asymmetrically reweighted penalized least squares smoothing. *Analyst* 140, 250.
- Bandfield, J.L., Hamilton, V.E., Christensen, P.R., McSweeney, H.Y., 2004. Identification of quartzofeldspathic materials on Mars. *J. Geophys. Res.* 109.
- Bandfield, J.L., Glotch, T.D., Christensen, P.R., 2003. Spectroscopic identification of carbonates in the martian dust. *Science* 301, 1084–1087.
- Bersch, M.G., Taylor, G.J., Keil, K., Norman, M.D., 1991. Mineral compositions in pristine lunar highland rocks and the diversity of highland magmatism. *Geophys. Res. Lett.* 18, 2085–2088.
- Bishop, J.L., Alpers, C.N., Coleman, M.L., Sobron, P., Lane, M.D., Dyar, M.D., Schiffman, P., 2008. Sulfates on Mars: comparison with spectral properties of analog sites. *Geochim. Cosmochim. Acta* 72, A85, A85.
- Blake, D.F., Morris, R.V., Kocurek, G., Morrison, S.M., Downs, R.T., Bish, D., Ming, D.W., Edgett, K.S., Rubin, D., Goetz, W., Madsen, M.B., Sullivan, R., Gellert, R., Campbell, I., Treiman, A.H., McLennan, S.M., Yen, A.S., Grotzinger, J., Vaniman, D.T., Chipera, S.J., Achilles, C.N., Rampe, E.B., Sumner, D., Meslin, P.Y., Maurice, S., Forni, O., Gasnault, O., Fisk, M., Schmidt, M., Mahaffy, P., Leshin, L.A., Glavin, D., Steele, A., Freissinet, C., Navarro-Gonzalez, R., Yingst, R.A., Kah, L.C., Bridges, N., Lewis, K.W., Bristow, T.F., Farmer, J.D., Crisp, J.A., Stolper, E.M., Marais, D.J.D., Sarrazin, P., Team, M.S., 2013. Curiosity at Gale Crater, Mars: characterization and analysis of the rocknest sand shadow. *Science* 341.
- Bost, N., Westall, F., Ramboz, C., Foucher, F., Pullan, D., Meunier, A., Petit, S., Fleischer, I., Klingelhöfer, G., Vago, J.L., 2013. Missions to Mars: characterisation of Mars analogue rocks for the International Space Analogue Rockstore (ISAR). *Planet. Space Sci.* 82–83, 113–127.
- Bost, N., Ramboz, C., Breton, N.L., Foucher, F., Lopez-Reyes, G., Angelis, S.D., Josset, M., Venegas, G., Sanz-Arraz, A., Pérez, F.R., Medina, J., Josset, J.-L., Souchon, A., Ammannito, E., Carli, C., Vago, J.L., Westall, F., 2015. Testing the ability of the ExoMars 2018 payload to document geological context and potential habitability on Mars. *Planet. Space Sci.* 108, 87–97.
- Boynton, W.V., Ming, D.W., Kounaves, S.P., Young, S.M.M., Arvidson, R.E., Hecht, M.H., Hoffman, J., Niles, P.B., Hamara, D.K., Quinn, R.C., Smith, P.H., Sutter, B., Catling, D.C., Morris, R.V., 2009. Evidence for calcium carbonate at the Mars Phoenix landing site. *Science* 325, 61–64.
- Brock, T.D., 1967. Life at high temperatures. *Science* 158, 1012–1019.
- Cahill, J.T., Floss, C., Anand, M., Taylor, L.A., Nazarov, M.A., Cohen, B.A., 2004. Petrogenesis of lunar highlands meteorites: Dhofar 025, Dhofar 081 Dar al Gani 262, and Dar al Gani 400. *Meteorit. Planet. Sci.* 39, 503–529.
- Christensen, P.R., McSweeney, H.Y., Bandfield, J.L., Ruff, S.W., Rogers, A.D., Hamilton, V.E., Gorelick, N., Wyatt, M.B., Jakosky, B.M., Kieffer, H.H., Malin, M.C., Moersch, J.E., 2005. Evidence for magmatic evolution and diversity on Mars from infrared observations. *Nature* 436, 504–509.
- Clark, B.C., Arvidson, R.E., Gellert, R., Morris, R.V., Ming, D.W., Richter, L., Ruff, S.W., Michalski, J.R., Farrand, W.H., Yen, A., Herkenhoff, K.E., Li, R., Squyres, S.W., Schroder, C., Klingelhofer, G., Bell, J.F., 2007. Evidence for montmorillonite or its compositional equivalent in the Columbia Hills, Mars. *J. Geophys. Res.* 112.
- Cloutis, E.A., McCormack, K.A., Bell III, J.F., Hendrix, A.R., Bailey, D.T., Craig, M.A., Mertzman, S.A., Robinson, M.S., Riner, M.A., 2008. Ultraviolet spectral reflectance properties of common planetary materials. *Icarus* 197, 321–347.
- Cockell, C.S., Lee, P., 2002. The biology of impact craters – a review. *Biol. Rev.* 77, 279–310.
- Cockell, C.S., Lee, P., Osinski, G., Horneck, G., Broady, P., 2002. Impact-induced microbial endolithic habitats. *Meteorit. Planet. Sci.* 37, 1287–1298.
- Cockell, C.S., Osinski, G.R., Lee, P., 2003. The impact crater as a habitat: effects of impact processing of target materials. *Astrobiology* 3, 181–191.
- Dhingra, D., Pieters, C.M., Boardman, J.W., Head, J.W., Isaacson, P.J., Taylor, L.A., 2011. Theophilus Crater: understanding the geological context of Mg-spinel bearing central peaks. *Geophys. Res. Lett.* 38, L1201.
- Donaldson Hanna, K.L., Thomas, I.R., Bowles, N.E., Greenhagen, B.T., Pieters, C.M., Mustard, J.F., Jackson, C.R.M., Wyatt, M.B., 2012a. Laboratory emissivity measurements of the plagioclase solid solution series under varying environmental conditions. *J. Geophys. Res.* 117, E11004.
- Donaldson Hanna, K.L., Wyatt, M.B., Thomas, I.R., Bowles, N.E., Greenhagen, B.T., Maturilli, A., Helbert, J., Paige, D.A., 2012b. Thermal infrared emissivity measurements under a simulated lunar environment: application to the diviner lunar radiometer experiment. *J. Geophys. Res.* 117, E00H05.
- Dowty, E., Prinz, M., Keil, K., 1974. Ferroan anorthosite-widespread and distinctive lunar rock type. *Earth Planet. Sci. Lett.* 24, 15–25.
- Ehlmann, B.L., Mustard, J.F., Murchie, S.L., Poulet, F., Bishop, J.L., Brown, A.J., Calvin, W.M., Clark, R.N., Des Marais, D.J., Milliken, R.E., Roach, L.H., Roush, T.L., Swayze, G.A., Wray, J.J., 2008. Orbital identification of carbonate-bearing rocks on Mars. *Science* 322, 1828–1832.
- Ehlmann, B.L., Mustard, J.F., Murchie, S.L., Bibring, J.P., Meunier, A., Fraeman, A.A., Langevin, Y., 2011. Subsurface water and clay mineral formation during the early history of Mars. *Nature* 479, 53–60.
- Fernandez-Remolar, D.C., Prieto-Ballesteros, O., Amils, R., Gomez, F., Friedlander, L., Arvidson, R., Morris, R.V., Gomez, D., 2009. Production of phyllosilicates and sulfates on Mars through acidic weathering: the Rio Tinto Mars analog model. *Bioastronomy 2007: Mol. Microbes, Extrater. Life* 420, 129–136.
- Gaddis, L., Pieters, C.M., Hawke, B.R., 1985. Remote sensing of lunar pyroclastic mantling deposits. *Icarus* 61, 461–489.
- Gendrin, A., Mangold, N., Bibring, J.P., Langevin, Y., Gondet, B., Poulet, F., Bonello, G., Quantin, C., Mustard, J., Arvidson, R., LeMouelic, S., 2005. Sulfates in martian layered terrains: the OMEGA/Mars express view. *Science* 307, 1587–1591.
- Glotch, T.D., Lucey, P.G., Bandfield, J.L., Greenhagen, B.T., Thomas, I.R., Elphic, R.C., Bowles, N., Wyatt, M.B., Allen, C.C., Hanna, K.D., Paige, D.A., 2010. Highly silicic compositions on the moon. *Science* 329, 1510–1513.
- Glotch, T.D., Morris, R.V., Christensen, P.R., Sharp, T.G., 2004. Effect of precursor mineralogy on the thermal infrared emission spectra of hematite: application to Martian hematite mineralization. *J. Geophys. Res.* 109.
- Gough, R.V., Chevrier, V.F., Baustain, K.J., Wise, M.E., Tolbert, M.A., 2011. Laboratory studies of perchlorate phase transitions: support for metastable aqueous perchlorate solutions on Mars. *Earth Planet. Sci. Lett.* 312, 371–377.
- Greenhagen, B.T., Lucey, P.G., Wyatt, M.B., Glotch, T.D., Allen, C.C., Arnold, J.A., Bandfield, J.L., Bowles, N.E., Hanna, K.L.D., Hayne, P.O., Song, E., Thomas, I.R., Paige, D.A., 2010. Global silicate mineralogy of the moon from the diviner lunar radiometer. *Science* 329, 1507–1509.
- Grotzinger, J.P., Sumner, D.Y., Kah, L.C., Stack, K., Gupta, S., Edgar, L., Rubin, D., Lewis, K., Schieber, J., Mangold, N., Milliken, R., Conrad, P.G., Desmarais, D., Farmer, J., Siebach, K., Calef 3rd, F., Hurowitz, J., McLennan, S.M., Ming, D., Vaniman, D., Crisp, J., Vasavada, A., Edgett, K.S., Malin, M., Blake, D., Gellert, R., Mahaffy, P., Wiens, R.C., Maurice, S., Grant, J.A., Wilson, S., Anderson, R.C., Beegle, L., Arvidson, R., Hallet, B., Sletten, R.S., Rice, M., Bell 3rd, J., Griffes, J., Ehlmann, B., Anderson, R.B., Bristow, T.F., Dietrich, W.E., Dromart, G., Eigenbrode, J., Fraeman, A., Hardgrove, C., Herkenhoff, K., Jandura, L., Kocurek, G., Lee, S., Leshin, L.A., Leveille, R., Limonadi, D., Maki, J., McCloskey, S., Meyer, M., Miniti, M., Newsom, H., Oehler, D., Okon, A., Palucis, M., Parker, T., Rowland, S., Schmidt, M., Squyres, S., Steele, A., Stolper, E., Summons, R., Treiman, A., Williams, R., Yingst, A., Team, M.S., 2013. A habitable fluvio-lacustrine environment at Yellowknife Bay, Gale Crater, Mars. *Science*.
- Hamilton, V.E., Christensen, P.R., 2005. Evidence for extensive, olivine-rich bedrock on Mars. *Geology* 33, 433–436.
- Hamilton, V.E., Christensen, P.R., Bandfield, J.L., 2003. Volcanism or aqueous alteration on Mars? *Nature* 421, 711–712.
- Hamilton, V.E., McSweeney, H.Y., Hapke, B., 2005. Mineralogy of Martian atmospheric dust inferred from thermal infrared spectra of aerosols. *J. Geophys. Res.* 110.
- Haskin, L.A., Gillis, J.J., Korotev, R.L., Jolliff, B.L., 2000. The materials of the lunar Procellarum KREEP Terrane: a synthesis of data from geomorphological mapping, remote sensing, and sample analyses. *J. Geophys. Res.* 105, 20403–20415.
- Horgan, B.H., Bell III, J.F., Noe Dobrea, E.Z., Cloutis, E.A., Bailey, D.T., Craig, M.A., Roach, L.H., Mustard, J.F., 2009. The distribution of hydrated minerals in the north polar regions of Mars. *J. Geophys. Res.* 114, E1005.
- Hui, H., Plesier, A.H., Zhang, Y., Neal, C.R., 2013. Water in lunar anorthosites and evidence for a wet early Moon. *Nat. Geosci.* 6, 177–180.
- Hurowitz, J.A., McLennan, S.M., Tosca, N.J., Arvidson, R.E., Michalski, J.R., Ming, D.W., Schroder, C., Squyres, S.W., 2006. In situ and experimental evidence for acidic weathering of rocks and soils on Mars. *J. Geophys. Res.* 111.
- Izawa, M.R.M., Banerjee, N.R., Osinski, G.R., Flemming, R.L., Parnell, J., Cockell, C.S., 2011. Weathering of post-impact hydrothermal deposits from the Haughton impact structure: implications for microbial colonization and biosignature preservation. *Astrobiology* 11, 537–550.
- Johnson, J.R., Bell III, J.F., Bender, S., Blaney, D., Cloutis, E.A., DeFlores, L., Ehlmann, B., Gasnault, O., Gondet, B., Kinch, K., Lemmon, M., Le Mouélic, S., Maurice, S., Rice, M.S., Wiens, R.C., Team, M.S., 2013. ChemCam passive reflectance spectroscopy of surface materials at the curiosity landing site, Mars. *Icarus*, under review.
- Jolliff, B.L., Gillis, J.J., Haskin, L.A., Korotev, R.L., Wiczorek, M.A., 2000. Major lunar crustal terranes: surface expressions and crust–mantle origins. *J. Geophys. Res.* 105, 4197–4216.
- Keil, K., Prinz, M., Bunch, T.E., 1970. Mineral chemistry of lunar samples. *Science* 167, 597 &.
- Keil, K., Warner, R.D., Prinz, M., Dowty, E., 1975. Rocks 60618 and 65785-evidence for admixture of kREEP in lunar impact melts. *Geophys. Res. Lett.* 2, 369–372.
- Knoll, A.H., Jolliff, B.L., Farrand, W.H., Bell, J.F., Clark, B.C., Gellert, R., Golombek, M.P., Grotzinger, J.P., Herkenhoff, K.E., Johnson, J.R., McLennan, S.M., Morris, R., Squyres, S.W., Sullivan, R., Tosca, N.J., Yen, A., Learner, Z., 2008. Veneers, rinds, and fracture fills: relatively late alteration of sedimentary rocks at Meridiani Planum, Mars. *J. Geophys. Res.* 113.
- Koeppen, W.C., Hamilton, V.E., 2008. Global distribution, composition, and abundance of olivine on the surface of Mars from thermal infrared data. *J. Geophys. Res.* 113.
- Korotev, R.L., 1991. Geochemical stratigraphy of 2 Regolith Cores from the central highlands of the Moon. *Proc. Lunar Planet. Sci.* 21, 229–289.
- Korotev, R.L., 2005. Lunar geochemistry as told by lunar meteorites. *Chem. Der Erde-geochem.* 65, 297–346.
- Korotev, R.L., Gillis, J.J., 2001. A new look at the Apollo 11 regolith and KREEP. *J. Geophys. Res.* 106, 12339–12353.

- Korotev, R.L., Jolliff, B.L., Zeigler, R.A., Gillis, J.J., Haskin, L.A., 2003. Feldspathic lunar meteorites and their implications for compositional remote sensing of the lunar surface and the composition of the lunar crust. *Geochim. Cosmochim. Acta* 67, 4895–4923.
- Korotev, R.L., Morris, R.V., 1993. Composition and maturity of Apollo 16 Regolith core 60013/14. *Geochim. Cosmochim. Acta* 57, 4813–4826.
- Korotev, R.L., Zeigler, R.A., Floss, C., 2010. On the origin of impact glass in the Apollo 16 regolith. *Geochim. Cosmochim. Acta* 74, 7362–7388.
- Korotev, R.L., Zeigler, R.A., Jolliff, B.L., Irving, A.J., Bunch, T.E., 2009. Compositional and lithological diversity among brecciated lunar meteorites of intermediate iron concentration. *Meteorit. Planet. Sci.* 44, 1287–1322.
- Kounaves, S.P., Hecht, M.H., Kapit, J., Quinn, R.C., Catling, D.C., Clark, B.C., Ming, D.W., Gospodinova, K., Hredzak, P., McElhoney, K., Shusterman, J., 2010. Soluble sulfate in the martian soil at the Phoenix landing site. *Geophys. Res. Lett.* 37.
- Le Bas, M.J., Le Maitre, R.W., Steckheisen, A., Zanettin, B., 1986. A chemical classification of volcanic rocks based on the total alkali–silica diagram. *J. Pet.* 27, 745–750.
- Leshin, L.A., Vicenzi, E., 2006. Aqueous processes recorded by Martian meteorites: analyzing Martian water on Earth. *Elements* 2, 157–162.
- Logan, L.M., Hunt, G.R., Salisbury, J.W., Balsamo, S.R., 1978. Compositional implications of Christiansen frequency maximums for infrared remote sensing applications. *J. Geophys. Res.* 78, 4983–5003.
- Lucey, P.G., 2004. Mineral maps of the Moon. *Geophys. Res. Lett.* 31 (8).
- McCord, T.B., Taylor, L.A., Combe, J.-P., Kramer, G., Pieters, C.M., Sunshine, J.M., Clark, R.N., 2011. Sources and physical processes responsible for OH/H₂O in the lunar soil as revealed by the Moon Mineralogy Mapper (M³). *J. Geophys. Res.* 116, 116–155.
- McCubbin, F.M., Steele, A., Hauri, E.H., Nekvasil, H., Yamashita, S., Hemley, R.J., 2010. Nominally hydrous magmatism on the Moon. *Proc. Natl. Acad. Sci. USA* 27, 11223–11228.
- McKeown, N.K., Bishop, J.L., Noe Dobra, E.Z., Ehlmann, B.L., Parente, M., Mustard, J.F., Murchie, S.L.S., G. A., Bibring, J.-P., Silver, E.A., 2009. Characterization of phyllosilicates observed in the central Marwth Vallis region, Mars, their potential formational processes, and implications for past climate. *J. Geophys. Res.* 114, 1–20.
- McLennan, S.M., Anderson, R.B., Bell 3rd, J.F., Bridges, J.C., Calef 3rd, F., Campbell, J.L., Clark, B.C., Clegg, S., Conrad, P., Cousin, A., Des Marais, D.J., Dromart, G., Dyar, M.D., Edgar, L.A., Ehlmann, B.L., Fabre, C., Forni, O., Gasnault, O., Gellert, R., Gordon, S., Grant, J.A., Grotzinger, J.P., Gupta, S., Herkenhoff, K.E., Hurowitz, J.A., King, P.L., Le Mouélic, S., Leshin, L.A., Leveille, R., Lewis, K.W., Mangold, N., Maurice, S., Ming, D.W., Morris, R.V., Nachon, M., Newsom, H.E., Ollila, A.M., Perrett, G.M., Rice, M.S., Schmidt, M.E., Schwenzer, S.P., Stack, K., Stolper, E.M., Sumner, D.Y., Treiman, A.H., Vanbommel, S., Vaniman, D.T., Vasavada, A., Wiens, R.C., Yingst, R.A., 2013. Elemental geochemistry of sedimentary rocks at Yellowknife Bay, Gale Crater, Mars. *Science*.
- McLennan, S.M., Bell, J.F., Calvin, W.M., Christensen, P.R., Clark, B.C., de Souza, P.A., Farmer, J., Farrand, W.H., Fike, D.A., Gellert, R., Ghosh, A., Glotch, T.D., Grotzinger, J.P., Hahn, B., Herkenhoff, K.E., Hurowitz, J.A., Johnson, J.R., Johnson, S.S., Jolliff, B., Klingelhofer, G., Knoll, A.H., Learner, Z., Malin, M.C., McSween, H.Y., Pockock, J., Ruff, S.W., Soderblom, L.A., Squyres, S.W., Tosca, N.J., Watters, W.A., Wyatt, M.B., Yen, A., 2005. Provenance and diagenesis of the evaporite-bearing Burns formation, Meridiani Planum, Mars. *Earth Planet. Sci. Lett.* 240, 95–121.
- McSween, H.Y., Taylor, G.J., Wyatt, M.-B., 2009. Elemental composition of the Martian crust. *Science* 324, 736–739.
- McSween, H.Y., Treiman, A.H., 1998. *Martian Meteorites*. In: *Papike, J.J., Planetary Materials*.
- Mertzman, S.A., 2000. K–Ar results from the southern Oregon–northern California Cascade Range. *Or. Geol.* 62, 99–122.
- Michalski, J.R., Niles, P.B., 2010. Deep crustal carbonate rocks exposed by meteor impact on Mars. *Nat. Geosci.* 3, 751–755.
- Milam, K.A., McSween, H.Y., Christensen, P.R., 2007. Plagioclase compositions derived from thermal emission spectra of compositionally complex mixtures: implications for Martian feldspar mineralogy. *J. Geophys. Res.* 112.
- Milam, K.A., McSween, H.Y., Moersch, J., Christensen, P.R., 2010. Distribution and variation of plagioclase compositions on Mars. *J. Geophys. Res.* 115.
- Ming, D.W., Archer Jr., P.D., Glavin, D.P., Eigenbrode, J.L., Franz, H.B., Sutter, B., Brunner, A.E., Stern, J.C., Freissinet, C., McAdam, A.C., Mahaffy, P.R., Cabane, M., Coll, P., Campbell, J.L., Atreya, S.K., Niles, P.B., Bell 3rd, J.F., Bish, D.L., Brinckerhoff, W.B., Buch, A., Conrad, P.G., Des Marais, D.J., Ehlmann, B.L., Fairen, A.G., Farley, K., Flesch, G.J., Francois, P., Gellert, R., Grant, J.A., Grotzinger, J.P., Gupta, S., Herkenhoff, K.E., Hurowitz, J.A., Leshin, L.A., Lewis, K.W., McLennan, S.M., Miller, K.E., Moersch, J., Morris, R.V., Navarro-Gonzalez, R., Pavlov, A.A., Perrett, G.M., Pradler, I., Squyres, S.W., Summons, R.E., Steele, A., Stolper, E.M., Sumner, D.Y., Szopa, C., Teinturier, S., Trainer, M.G., Treiman, A.H., Vaniman, D.T., Vasavada, A.R., Webster, C.R., Wray, J.J., Yingst, R.A., 2013. Volatile and organic compositions of sedimentary rocks in Yellowknife Bay, Gale Crater, Mars. *Science*.
- Ming, D.W., Mittlefehldt, D.W., Morris, R.V., Golden, D.C., Gellert, R., Yen, A., Clark, B.C., Squyres, S.W., Farrand, W.H., Ruff, S.W., Arvidson, R.E., Klingelhofer, G., McSween, H.Y., Rodionov, D.S., Schroder, C., de Souza, P.A., Wang, A., 2006. Geochemical and mineralogical indicators for aqueous processes in the Columbia Hills of Gusev crater, Mars. *J. Geophys. Res.* 111.
- Morris, R.V., Klingelhofer, G., Schroder, C., Fleischer, I., Ming, D.W., Yen, A.S., Gellert, R., Arvidson, R.E., Rodionov, D.S., Crumpler, L.S., Clark, B.C., Cohen, B.A., McCoy, T.J., Mittlefehldt, D.W., Schmidt, M.E., de Souza, P.A., Squyres, S.W., 2008. Iron mineralogy and aqueous alteration from Husband Hill through Home Plate at Gusev Crater, Mars: results from the Mossbauer instrument on the Spirit Mars Exploration Rover. *J. Geophys. Res.* 113.
- Morris, R.V., Klingelhofer, G., Schroder, C., Rodionov, D.S., Yen, A., Ming, D.W., de Souza, P.A., Fleischer, I., Wdowiak, T., Gellert, R., Bernhardt, B., Evlanov, E.N., Zubkov, R.E., Foh, J., Bonnes, U., Kankeleit, E., Gutlich, P., Renz, F., Squyres, S.W., Arvidson, R.E., 2006. Mossbauer mineralogy of rock, soil, and dust at Gusev crater, Mars: Spirit's journey through weakly altered olivine basalt on the plains and pervasively altered basalt in the Columbia Hills. *J. Geophys. Res.* 111.
- Morris, R.V., Ruff, S.W., Gellert, R., Ming, D.W., Arvidson, R.E., Clark, B.C., Golden, D.C., Siebach, K., Klingelhofer, G., Schroeder, C., Fleischer, I., Yen, A.S., Squyres, S.W., 2010. Identification of carbonate-rich outcrops on Mars by the Spirit Rover. *Science* 329, 421–424.
- Mustard, J.F., Murchie, S.L., Pelkey, S.M., Ehlmann, B.L., Milliken, R.E., Grant, J.A., Bibring, J.P., Poulet, F., Bishop, J., Dobra, E.N., Roach, L., Seelos, F., Arvidson, R.E., Wiseman, S., Green, R., Hash, C., Humm, D., Malaret, E., McGovern, J.A., Seelos, K., Clancy, T., Clark, R., Des Marais, D., Izenberg, N., Knudson, A., Langevin, Y., Martin, T., McGuire, P., Morris, R., Robinson, M., Roush, T., Smith, M., Swayze, G., Taylor, H., Titus, T., Wolff, M., 2008. Hydrated silicate minerals on Mars observed by the Mars reconnaissance orbiter CRISM instrument. *Nature* 454, 305–309.
- Nash, D.B., Salisbury, J.W., Conel, J.E., Lucey, P.G., Christensen, P.R., 1993. Evaluation of infrared-emission spectroscopy for mapping the Moons surface-composition from Lunar Orbit. *J. Geophys. Res.* 98, 23535–23552.
- Niles, P.B., Michalski, J., 2009. Meridiani Planum sediments on Mars formed through weathering in massive ice deposits. *Nat. Geosci.* 2, 215–220.
- Norman, M.D., Taylor, G.J., Keil, K., 1991. Additional complexity in the lunar crust-petrology of sodic anorthosites and sulfur-rich, ferroan noritic anorthosites. *Geophys. Res. Lett.* 18, 2081–2084.
- Ohtake, M., Matsunaga, T., Haruyama, J., Yokota, Y., Morota, T., Honda, C., Ogawa, Y., Torii, M., Miyamoto, H., Arai, T., Hirata, N., Iwasaki, A., Nakamura, R., Hiroi, T., Sugihara, T., Takeda, H., Otake, H., Pieters, M.C., Saiki, K., Kitazato, K., Abe, M., Asada, N., Demura, H., Yamaguchi, Y., Sasaki, S., Kodama, S., Terazono, J., Shirao, M., Yamaji, A., Minami, S., Akiyama, H., Josset, J.-L., 2009. The global distribution of pure anorthosite on the Moon. *Nature* 461, 236.
- Nyquist, L.E., Bogard, D.D., Shih, C.-Y., Greshake, A., Stöffler, D., Eugster, O., 2001. Ages and geologic histories of Martian meteorites. *Space Sci. Rev.* 96, 105–164.
- Osinski, G.R., Lee, P., Parnell, J., Spray, J.G., Baron, M.T., 2005. A case study of impact-induced hydrothermal activity: the Haughton impact structure, Devon Island, Canadian high arctic. *Meteorit. Planet. Sci.* 40, 1859–1877.
- Oze, C., Sharma, M., 2005. Have olivine, will gas: serpentinization and the abiogenic production of methane on Mars. *Geophys. Res. Lett.* 32, L10203–L10207.
- Palomba, E., Zinzi, A., Cloutis, E.A., D'Amore, M., Grassi, D., Maturilli, A., 2009. Evidence for Mg-rich carbonates on Mars from a 3.9 μm absorption band. *Icarus* 203, 58–65.
- Papike, J.J., Karner, J.M., Shearer, C.K., 2003. Determination of planetary basalt parentage: a simple technique using the electron microprobe. *Am. Mineral.* 88, 469–472.
- Papike, J.J., Ryder, G., Shearer, C.K., 1998. Lunar samples. In: *Papike, J.J. (Ed.), Planetary Materials*. Mineralogical Society of America, Washington, DC.
- Pieters, C.M., Besse, S., Boardman, J., Buratti, B., Cheek, L., Clark, R.N., Combe, J.P., Dhingra, D., Goswami, J.N., Green, R.O., Head, J.W., Isaacson, P., Klima, R.L., Kramer, G., Lundeen, S., Malaret, E., McCord, T.B., Mustard, J.F., Nettles, J., Petro, N., Runyon, C., Staid, M.I., Sunshine, J.M., Taylor, C., Thaisen, K.G., Tompkins, S., Whitten, J., 2011. Mg-spinel lithology: a new rock type on the lunar farside. *J. Geophys. Res.* 116, 1–14.
- Pieters, C.M., Donaldson Hanna, K., Cheek, L., Dhingra, D., Prissel, T., Jackson, C., Moriarty, D., Parman, S., Taylor, L.A., 2014. The distribution of Mg-spinel across the Moon and constraints on crustal origin. *Am. Mineral.*, 1893–1910, October 99.
- Pieters, C.M., Goswami, J.N., Clark, R.N., Annadurai, M., Boardman, J., Buratti, B., Combe, J.-P., Dyar, M.D., Green, R., Head, J.W., Hibbitts, C.A., Hicks, M., Isaacson, P., Klima, R.L., Kramer, R., Kumar, S., Livo, E., Lundeen, S., Malaret, E., McCord, T.B., Mustard, J.F., Nettles, J., Petro, N., Runyon, C., Staid, M.I., Sunshine, J.M., Taylor, L.A., Tompkins, S., Varanasi, P., 2009. Character and spatial distribution of OH/H₂O on the surface of the Moon seen by M3 on Chandrayaan-1. *Science* 326, 568–572.
- Reichen, L.E., Fahey, J.J., 1962. An improved method for the determination of FeO in rocks and minerals including garnet. *U.S. Geol. Surv. Bull.* 1144B, 1–5.
- Rice, M.S., Bell III, J.F., Cloutis, E.A., Wang, A., Ruff, S.W., Craig, M.A., Bailey, D.T., Johnson, J.R., de Souza, P.A., Farrand, W.H., 2009. Silica-rich deposits and hydrated minerals at Gusev crater, Mars: Vis-NIR spectral characterization and regional mapping. *Icarus* 205, 119–133.
- Ringwood, A.E., Green, D.H., 1972. Crystallization of plagioclase in lunar basalts and its significance. *Earth Planet. Sci. Lett.* 14, 14 &.
- Robertson, K., Bish, D., 2011. Stability of phases in the Mg(ClO₄)₂ · nH₂O system and implications for perchlorate occurrences on Mars. *J. Geophys. Res.* 116, E07006.
- Rogers, A.D., Bandfield, J.L., Christensen, P.R., 2007. Global spectral classification of martian low-albedo regions with MGS-TES data. *J. Geophys. Res. – Planets* 112, E02004. <http://dx.doi.org/10.1029/2006JE002726>.
- Rogers, A.D., Aharonson, O., 2008. Mineralogical composition of sands in Meridiani Planum determined from Mars Exploration Rover data and comparison to orbital measurements. *J. Geophys. Res.* 113.
- Rogers, A.D., Christensen, P.R., 2007. Surface mineralogy of martian low-albedo regions from MGS-TES data: Implications for crustal evolution and surface alteration. *J. Geophys. Res. – Planets* 112, E01003. <http://dx.doi.org/10.1029/2006JE002727>.
- Ruff, S.W., Christensen, P.R., Barbera, P.W., Anderson, D.L., 1997. Quantitative thermal emission spectroscopy of minerals: a laboratory technique for measurement and calibration. *J. Geophys. Res.* 102, 14899–14913.
- Saal, A.E., Hauri, E.H., Cascio, M.L., van Orman, J.A., Rutherford, M.C., Cooper, R.F., 2008. Volatile content of lunar volcanic glasses and the presence of water in the Moon's interior. *Nature* 454, 192–195.
- Saal, A.E., Hauri, E.H., Van Orman, J.A., Rutherford, M.J., 2013. Hydrogen isotopes in lunar volcanic glasses and melt inclusions reveal a carbonaceous chondrite heritage. *Science* 14, 1317–1320.

- Salvatore, M.R., Mustard, J.F., Head, J.W., Rogers, A.D., Cooper, R.F., 2014. The dominance of cold and dry alteration processes on recent Mars, as revealed through pan-spectral orbital analyses. *Earth Planet. Sci. Lett.* 404, 261–272.
- Schwenzer, S.P., Abramov, O., Allen, C.C., Clifford, S.M., Cockell, C.S., Filiberto, J., Kring, D.A., Lasue, J., McGovern, P.J., Newsom, H.E., Treiman, A.H., Vaniman, D.T., Wiens, R.C., 2012. Puncturing Mars: how impact craters interact with the Martian cryosphere. *Earth Planet. Sci. Lett.* 335–336, 9–17.
- Schwenzer, S.P., Kring, D.A., 2009. Impact-generated hydrothermal systems capable of forming phyllosilicates on Noachian Mars. *Geology* 37, 1091–1094.
- Shirley, K.A., Glotch, T.D., 2015. First measurements from the Planetary and Asteroid Regolith spectroscopy environmental chamber (PARSEC). *Lunar Planet. Sci.*, XLVI, abstract 2025
- Seddio, S.M., Jolliff, B.L., Korotev, R.L., Zeigler, R.A., 2013. Petrology and geochemistry of lunar granite 12032, 366-19 and implications for lunar granite petrogenesis. *Am. Mineral.* 98, 1697–1713.
- Smith, D.L., Samson, C., Herd, R., Deslauriers, A., Sink, J.-E., Christie, I., Ernst, R.E., 2006. Measuring the bulk density of meteorites nondestructively using three-dimensional laser imaging. *J. Geophys. Res.* 111, E10002.
- Song, E., Bandfield, J.L., Lucey, P.G., Greenhagen, B.T., Paige, D.A., 2013. Bulk mineralogy of lunar crater central peaks via thermal infrared spectra from the Diviner Lunar Radiometer: a study of the Moon's crustal composition at depth. *J. Geophys. Res.* 118, 689–707.
- Spudis, P.D., Bussey, D.B.J., Baloga, S.M., Butler, B.J., Carl, D., Carter, L.M., Chakraborty, M., Elphic, R.C., Gillis-Davis, J.J., Goswami, J.N., Heggy, E., Hillyard, M., Jensen, R., Kirk, R.L., LaVallee, D., McKerracher, P., Neish, C.D., Nozette, S., Nylund, S., Palsetia, M., Patterson, W., Robinson, R.K., Schulze, R.C., Sequeira, H., Skura, J., Thompson, T.W., Thomson, B.J., Ustinov, E.A., Winters, H. L., 2010. Initial results for the north pole of the Moon from Mini-SAR, Chandrayaan-1 mission. *Geophys. Res. Lett.* 37 (6), L06204.
- Squyres, S.W., Arvidson, R.E., Bollen, D., Bell, J.F., Brückner, J., Cabrol, N.A., Calvin, W.M., Carr, M.H., Christensen, P.R., Clark, B.C., Crumpler, L., Des Marais, D.J., d'Uston, C., Economou, T., Farmer, J., Farrand, W.H., Folkner, W., Gellert, R., Glotch, T.D., Golombek, M., Gorevan, S., Grant, J.A., Greeley, R., Grotzinger, J., Herkenhoff, K.E., Hviid, S., Johnson, J.R., Klingelhöfer, G., Knoll, A.H., Landis, G., Lemmon, M., Li, R., Madsen, M.B., Malin, M.C., McLennan, S.M., McSween, H.Y., Ming, D.W., Moersch, J., Morris, R.V., Parker, T., Rice, J.W., Richter, L., Rieder, R., Schröder, C., Sims, M., Smith, M., Smith, P., Soderblom, L.A., Sullivan, R., Tosca, N.J., Wänke, H., Wdowiak, T., Wolff, M., Yen, A., 2006. Overview of the opportunity Mars exploration rover mission to Meridiani Planum: Eagle Crater to purgatory ripple. *J. Geophys. Res.* 111, CitelID E12S12.
- Squyres, S.W., Arvidson, R.E., Ruff, S., Gellert, R., Morris, R.V., Ming, D.W., Crumpler, L., Farmer, J.D., Des Marais, D.J., Yen, A., McLennan, S.M., Calvin, W., Bell, J.F., Clark, B.C., Wang, A., McCoy, T.J., Schmidt, M.E., de Souza, P.A., 2008. Detection of silica-rich deposits on Mars. *Science* 320, 1063–1067.
- Squyres, S.W., Grotzinger, J.P., Arvidson, R.E., Bell, J.F., Calvin, W., Christensen, P.R., Clark, B.C., Crisp, J.A., Farrand, W.H., Herkenhoff, K.E., Johnson, J.R., Klingelhofe, G., Knoll, A.H., McLennan, S.M., McSween, H.Y., Morris, R.V., Rice, J.W., Rieder, R., Soderblom, L.A., 2004. In situ evidence for an ancient aqueous environment at Meridiani Planum, Mars. *Science* 306, 1709–1714.
- Squyres, S.W., Knoll, A.H., 2005. Sedimentary rocks at Meridiani Planum: origin, diagenesis, and implications for life on Mars. *Earth Planet. Sci. Lett.* 240, 1–10.
- Steele, I.M., Smith, J.V., 1973. Compositional and x-ray data for Luna-20 Feldspar. *Geochim. Cosmochim. Acta* 37, 1075–1077.
- Sunshine, J.M., Farnham, T.L., Feaga, L.M., Groussin, O., Merlin, F., Milliken, R.E., A'Hearn, M.F., 2009. Temporal and spatial variability of lunar hydration as observed by the Deep Impact spacecraft. *Science* 326, 565–568.
- Tosca, N.J., McLennan, S.M., Clark, B.C., Grotzinger, J.P., Hurowitz, J.A., Knoll, A.H., Schroder, C., Squyres, S.W., 2005. Geochemical modeling of evaporation processes on Mars: insight from the sedimentary record at Meridiani Planum. *Earth Planet. Sci. Lett.* 240, 122–148.
- Vaniman, D.T., Bish, D.L., Ming, D.W., Bristow, T.F., Morris, R.V., Blake, D.F., Chipera, S.J., Morrison, S.M., Treiman, A.H., Rampe, E.B., Rice, M., Achilles, C.N., Grotzinger, J., McLennan, S.M., Williams, J., Bell 3rd, J., Newsom, H., Downs, R.T., Maurice, S., Sarrazin, P., Yen, A.S., Morookian, J.M., Farmer, J.D., Stack, K., Milliken, R.E., Ehlmann, B., Sumner, D.Y., Berger, G., Crisp, J.A., Hurowitz, J.A., Anderson, R., Desmarais, D., Stolper, E.M., Edgett, K.S., Gupta, S., Spanovich, N., Team, M.S., 2013. Mineralogy of a Mudstone at Yellowknife Bay, Gale Crater, Mars. *Science*.
- Viviano, C.E., Moersch, J.E., McSween, H.Y., 2013. Implications for early hydrothermal environments on Mars through the spectral evidence for carbonation and chloritization reactions in the Nili Fossae region. *J. Geophys. Res.* 118, 1858–1872.
- Wakita, H., Schmitt, R.A., 1971. Lunar Anorthosites-Plagioclase crystallization. *Science* 172, 184 &.
- Walker, D., Hays, J.F., 1977. Plagioclase flotation and lunar crust formation. *Geology* 5, 425–428.
- Wells, E., Hapke, B., 1977. Lunar soil-iron and titanium bands in glass fraction. *Science* 195, 977–979.
- Wells, E.N., Cassidy, W.A., Hapke, B.W., 1972. Lunar and laboratory glasses and spectrum of Moon. *Trans. Geophys. Union.* 53, 429.
- Williams, R.M., Grotzinger, J.P., Dietrich, W.E., Gupta, S., Sumner, D.Y., Wiens, R.C., Mangold, N., Malin, M.C., Edgett, K.S., Maurice, S., Forni, O., Gasnault, O., Ollila, A., Newsom, H.E., Dromart, G., Palucis, M.C., Yingst, R.A., Anderson, R.B., Herkenhoff, K.E., Le Mouelic, S., Goetz, W., Madsen, M.B., Koefoed, A., Jensen, J.K., Bridges, J.C., Schwenzer, S.P., Lewis, K.W., Stack, K.M., Rubin, D., Kah, L.C., Bell 3rd, J.F., Farmer, J.D., Sullivan, R., Van Beek, T., Blaney, D.L., Pariser, O., Deen, R.G., 2013. Martian fluvial conglomerates at Gale crater. *Science* 340, 1068–1072.
- Winchester, J.A., Floyd, P.A., 1977. Geochemical magma type discrimination: application to altered and metamorphosed basic igneous rocks. *Earth Planet. Sci. Lett.* 28, 459–469.
- Wray, J.J., Ehlmann, B.L., Squyres, S.W., Mustard, J.F., Kirk, R.L., 2008. Compositional stratigraphy of clay-bearing layered deposits at Mawrth Vallis, Mars. *Geophys. Res. Lett.* 35.
- Yamamoto, S., Nakamura, R., Matsunaga, T., Ogawa, Y., Ishihara, Y., Morata, T., Hirata, N., Ohtake, M., Hiroi, T., Yokota, Y., Haruyama, J., 2010. Possible mantle origin of olivine around lunar impact basins detected by SELENE. *Nat. Geosci.* 3, 533–536.